UMC Utrecht **Utrecht University**

Calcified cartilage tissue engineering: a comparison of hydroxyapatite and β-tricalcium phosphate bioinks

Author: Saraswati Bhushan
i6912672
s.bhushan@students.uu.nl

Supervisor: Dr. Miguel Castilho

June 2022

Table of Contents

Abstract

654 million people worldwide suffer from knee osteoarthritis, resulting in a reduced quality of life for patients and a burden on the healthcare system. Tissue engineering strategies represent a promising alternative to current surgical interventions in the repair of osteochondral tissue. Tissue engineering strategies have neglected the critical role of the calcified cartilage zone in providing a mechanically competent interphase between soft viscoelastic cartilage and stiff bone. This results in bi-phasic osteochondral scaffolds failing due to phase delamination and dislodgement. The aim of the present study is to propose a new bioink for engineering calcified cartilage tissue. Our study presents a comparison between a hydroxyapatite (HA)-based biomaterial ink and a β-tricalcium phosphate (β-TCP)-based biomaterial ink. While solvent-based extrusion printing has been used to fabricate HA- PCL (hydroxyapatite- polycaprolactone) scaffolds, to our knowledge, this technique has not been used for the fabrication of β-TCP-PCL scaffolds. Solvent-based extrusion printing can be performed at room temperature avoids the disadvantages associated with printing at high temperatures. The hypothesis is that β-TCP-PCL will induce chondrocyte hypertrophy and faster deposition of a mineralized calcified cartilage layer due to the higher solubility of β-TCP compared to HA. Our study is the first to show that the novel bioink composed of β-TCP-PCL can be processed with solvent-based extrusion printing in the same way as HA-PCL. The biomaterial inks with the highest ceramic concentrations (70%HA- 30% PCL and 70% β-TCP- 30% PCL) have the highest yield stress and consequently best shape fidelity, while printing resolution is similar with a minimum interfibre space of 0.5-1 mm for all concentrations of both groups. Solvent based extrusion printing can be used to print centimeter sized porous scaffolds with both materials (70%HA- 30% PCL and 70% β-TCP -30% PCL). Macropores were in the range of 300-900 um, which facilitates to bone ingrowth. We found that PCL does not mask the ceramic phase and there is a higher release of calcium and phosphorous ions from the β-TCP material. The *in vitro* experiments showed that cells remained viable and metabolically active over 28 days. In terms of the production of matrix components, small amounts of glycosaminoglycans were produced. Collagen type II was not produced by any of the groups, while Collagen type I was produced by all groups. It is possible that the chondrocytes de-differentiated and consequently produce fibrocartilage. However, to investigate whether the ceramic ions induce chondrocyte hypertrophy and the deposition of a mineralized matrix, a Collagen type X staining and ALP assay should be performed. Therefore, further investigation is required to truly conclude whether the higher soluble β-TCP results in the faster production of calcified cartilage.

Layman's summary

The human knee joint consists of two bones, the thigh bone and the shin bone, which are covered by a tissue called articular cartilage. The articular cartilage tissue cushions the joint and reduces friction between the bones, allowing them to glide against each other. It plays a critical role in the load bearing abilities of the knee joint. Cartilage is composed of only once cell type called chondrocytes and the extracellular matrix is composed of proteoglycans and collagen type II. Cartilage has no blood vessels or nerves, and chondrocytes have very limited proliferation, and consequently cartilage is virtually unable to self-heal. Trauma and aging can lead to degradation of cartilage (and other tissues in the knee joint) and result in a degenerative disease called osteoarthritis. Osteoarthritis affects over 654 million people worldwide and patients suffer from reduced mobility and consequently reduced quality of life. When cartilage is extensively damaged, patients must undergo a total knee replacement, an invasive surgery. The limited surgical options for cartilage repair has prompted scientists to explore tissue engineering solutions. Tissue engineering seeks to repair and restore damaged tissues using a combination of cells which are embedded in a biomaterial matrix known as a scaffold. Scaffolds structurally support cells and provide them cues for them to produce extracellular matrix components of neo-tissue. Tissue engineering often uses 3D printing to fabricate scaffolds, which prints 3D structures in a layer-by-layer manner using a so-called 'bioink'. A bioink must have biocompatible components and appropriate rheological properties (which deals with how well a material can flow and deform). The current tissue engineering studies focusing on cartilage still display weaker mechanical properties compared to native tissue. One reason for this is that tissue engineering studies have neglected the critical role of the calcified cartilage tissue layer. Soft and flexible cartilage is connected to stiff bone through an interface layer, which is called the calcified cartilage layer. This layer is critical in providing a mechanically competent interface and transmits various mechanical forces from cartilage to bone. Calcified cartilage has some matrix components contained in cartilage i.e. the presence of proteoglycans and collagen type II, and some matrix components of bone i.e. collagen type X and alkaline phosphatases.

Our study therefore focusses on engineering calcified cartilage tissue. We compare two scaffold bioinks, one of hydroxyapatite (HA) and one of β- tri-calcium phosphate (β-TCP). These materials resemble the inorganic component of bone tissue, and they release calcium and phosphorous ions. These ions provide cells the right cues to produce calcified cartilage tissue. Since β-TCP is more soluble than HA, we expect that it will release ions faster and enable the production of calcified cartilage extracellular matrix at a faster rate than HA. We use a special type of 3D printing called solvent-based extrusion printing to fabricate our scaffolds. The advantage of solvent-based extrusion printing is that it can be performed at room temperature, avoiding disadvantages associated with 3D printing at high temperatures. While it has been used previously to fabricate scaffolds composed of HA, it has not been used to produce scaffolds of β-TCP. First, we compared the rheological properties and printing resolution of various concentrations of these two bioinks. We found that the novel β-TCP bioink can be processed in the same way as a HA bioink using solvent-based extrusion printing. The novel β-TCP bioink displays the appropriate rheological characteristics and printing resolution. In addition, both the HA and β-TCP bioink can be used to 3D print scaffolds with the right pore size for this application. Further we confirmed that the release of calcium and phosphorous ions is indeed higher from a β-TCP scaffold compared to a HA scaffold. We performed an *in vitro* study to see if chondrocytes can be induced to produce calcified cartilage tissue by taking cues from the bioinks. The chondrocytes remain viable and metabolically active during the 28 days of *in vitro* culture. Two of the extracellular matrix components of calcified cartilage tissue, namely collagen type II and proteoglycans are produced in very small amounts by the cells. However, future studies should test for the production of characteristic markers of calcified cartilage, Collagen type X and alkaline phosphatases. Therefore, while the novel β-TCP bioink has the right rheological characteristics and produces scaffolds with the right pore size for calcified cartilage tissue engineering, further research is needed on the biological properties of the bioink. In conclusion, the present study is inconclusive in answering whether β-TCP is a superior bioink for engineering calcified cartilage.

1. INTRODUCTION

1.1. Anatomy of the osteochondral unit

Knees, hips, and finger joints are examples of diarthrodial joints. Diarthrodial joints are multi-tissue organs, which consist of two articulating bones, the articular cartilage layer covering the bones, the synovial lining, tendons, ligaments, and menisci. Diarthrodial joints, and knee joints, play a role in physical mobility and therefore impaired joint movement significantly impacts quality of life. The articular cartilage, calcified cartilage, and subchondral cortical and trabecular bone together form a bio composite, called the osteochondral unit. The components of the osteochondral unit are mechanically, biochemically, and physiologically interconnected. They are responsible for joint loading and weight bearing. Each component of the osteochondral unit consists of a unique structure, composition, and function, described in the sections below (Goldring & Goldring, 2016; Piluso et al., 2019).

1.1.1. Articular cartilage

Articular cartilage (AC) is a specialized connective tissue that covers the surfaces of joints and facilitates the transmission of loads, enabling friction free movement. In fact articular cartilage in the knee can support up to six times the body weight. Articular cartilage is an avascular, aneural and alymphatic tissue. It is a hypocellular tissue, composed in small percentage by cells called chondrocytes, which are surrounded by extracellular matrix. Chondrocytes, with a diameter of close to 13 µm, make up only 1-5% of the total tissue volume. Further, a small sub-population, comprising 0.1-1% of the tissue volume, of articular cartilage chondroprogenitor cells (ACPCs) are present in the superficial tangential zone. The remaining 95-99% of the tissue consists of extracellular matrix (ECM) components, which is 80% water and 20% solids (Camarero-Espinosa et al., 2016; Zhou et al., 2020).

The solid component of the ECM is composed of a fibrillar network of collagen (50-75%) embedded in a gel-like matrix of proteoglycans (15-30%). Articular cartilage is composed of zones, each with a unique arrangement of fibres, ECM components, and shape and arrangement of chondrocytes. The tissue comprises a superficial or tangential zone (SZ) (10-20% of cartilage thickness), middle zone (MZ) (40-60% of cartilage thickness), deep zone (DZ) and calcified zone (20-50% of cartilage thickness). Figure 1 indicates the anisotropic organization of ECM components and chondrocytes. In the superficial zone, the collagen fibres are parallel to the articulating surface and chondrocytes appear flattened and also parallel to the collagen fibres. The middle zone consists of collagen fibres organized into arcades and chondrocytes display a round morphology. In the and deep and calcified zones, collagen fibres are perpendicular to the subchondral bone and chondrocytes appear elongated and oriented in the direction of the collagen fibres (Camarero-Espinosa et al., 2016; Musumeci, 2016). The diameter of the collagen fibrils increases from the superficial zone to the deep zone, while the density of chondrocytes decreases from the superficial to the deep zone. In addition, the amount of glycosaminoglycans decreases from the superficial to deep zone (Doyle et al., 2021). Apart from the zonal arrangement of articular cartilage along the y axis, an additional microstructure is the chondron. The zonal arrangement of cartilage tissue and the structure of the chondron are shown in Figure 2 (Wei & Dai, 2021). Chondrocytes lack cell-cell interactions and are surrounded by a pericellular matrix, which is rich in proteoglycans, Collagen 6 and Collagen 9 (Camarero-Espinosa et al., 2016). Matrix synthesis is more prevalent in chondrons compared to the rest of the ECM (Abbadessa et al., 2016).

Being a biomechanical tissue, the compressive, shear and tensile properties of articular cartilage are due to its bi-phasic (fibrous and non-fibrous component) and viscoelastic nature. The compressive aggregate of cartilage ranges from 0.08 to 2 MPa and the Young's modulus ranges from 5 to 25 MPa. Both compressive and Young's moduli are higher in the superficial zone and reduce in the middle and deep zone (Camarero-Espinosa et al., 2016; B. Zhang et al., 2020). The other non-fibrous ECM component is proteoglycans. Proteoglycans consist of a core protein with covalently attached polysaccharide chains, mainly glycosaminoglycans (GAGs), which are perpendicular to the core protein. Figure 2 shows the main matrix components of articular cartilage and their structures (Wei & Dai, 2021). The most common GAGs are keratin sulphate, chondroitin-4-sulphate, chondroitin-6-sulphate, dermatan sulphate and hyaluronan. GAGs are negatively charged due to the presence of sulphate ester and carboxylic acid groups. This results in a fixed negative charge density of the ECM, which is responsible for attracting synovial fluid into the tissue and building osmotic pressure. Osmotic swelling, known as the Donan effect, is resisted by collagen fibres due to their high tensile strength, which limits the displacement of GAGs. This mechanism endows articular cartilage tissue with its unique

load bearing ability. In addition, collagen fibres provide resistance to shear stress in the superficial tangential zone (Camarero-Espinosa et al., 2016).
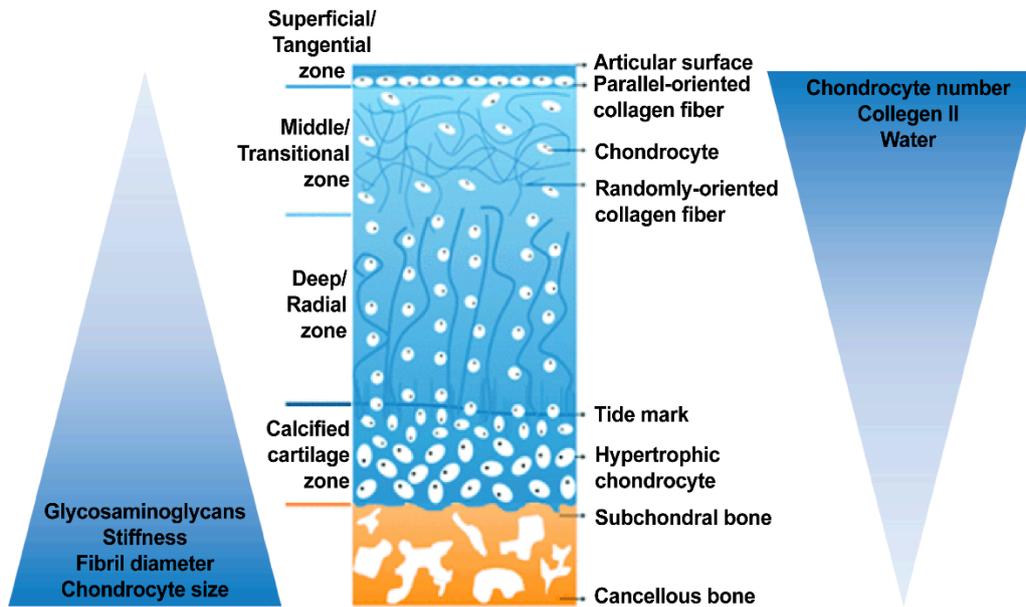

**Figure 1**: Zonal arrangement of the osteochondral unit (Doyle et al., 2021)
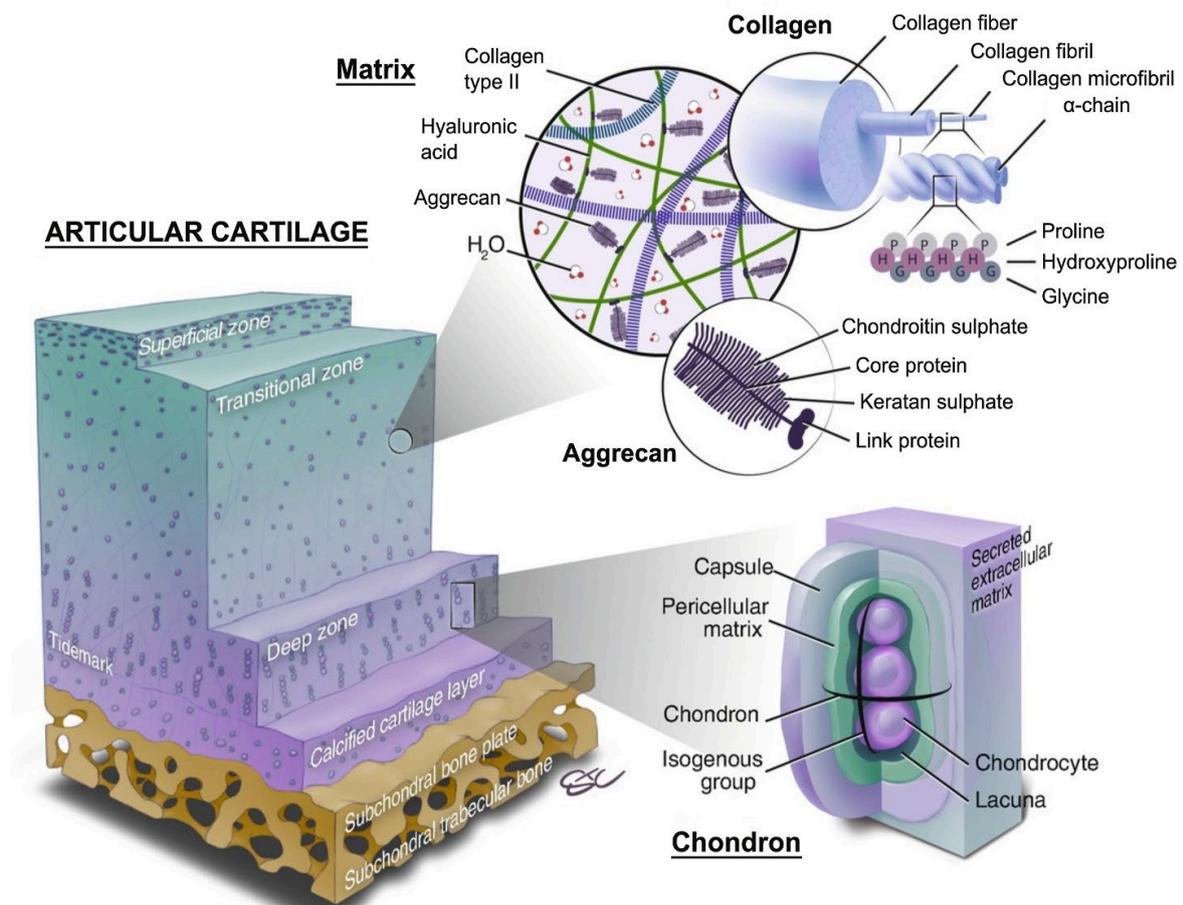
Figure 2: Articular cartilage matrix components and their structures (Wei & Dai, 2021)

1.1.2. Calcified cartilage

The calcified cartilage is a highly mineralized layer, which serves as an anchor between soft hyaline cartilage and the underlying subchondral bone (St-Pierre et al., 2012). This layer provides a stiffness transition between soft cartilage and stiffer bone and serves to transmit compressive, shear and tensile forces from the viscoelastic cartilage to the bone. To illustrate the difference in stiffness between the cartilage and bone, a comparison of their Young's moduli can be made. The modulus of articular cartilage is 1-15 MPa, that of calcified cartilage is 0.3 GPa and that of bone is 2 GPa (Farr & Gomoll, 2018). Compositionally, calcified cartilage consists of rounded hypertrophic chondrocytes secreting Collagen type X embedded in a hydroxyapatite matrix. The ECM of calcified cartilage also consists of Collagen type II and glycosaminoglycans, as well as alkaline phosphatases which are responsible for the hydroxyapatite deposition (Farr & Gomoll, 2018). Calcified cartilage is separated from the deep zone of cartilage by a thin tidemark layer. The tidemark layer is 5 µm thick discrete band of calcified cartilage, which can be histologically visualized with hematoxylin, as seen in Figure 3. The function of the tidemark layer is unclear, however, it is hypothesized that it prevents calcifying matrix vesicles produced from the bone from leaching into articular cartilage (Hoemann et al., 2012). While it was previously thought that the calcified cartilage layer was an impermeable barrier, there evidence of diffusion of small bioactive molecules from the cartilage to subchondral bone, thus this layer facilitates intracellular communication (Choe et al., 2021; Pouran et al., 2017).
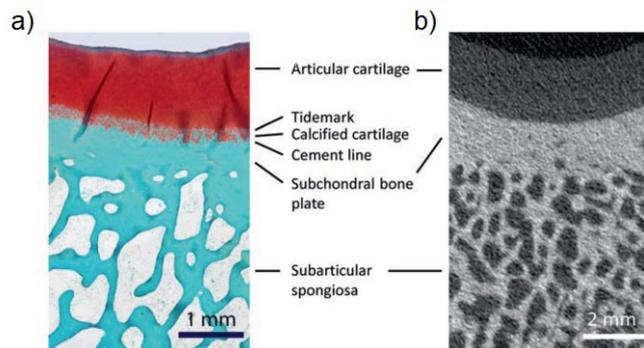

Figure 3: Safranin-O/ Fast green staining (left) and Micro CT figure (right) of the osteochondral unit (Farr & Gomoll, 2018)

1.1.3. Subchondral bone

The subchondral bone is separated from the calcified cartilage by a cement line. Bone is composed of water (10%), organic components (30%- mainly Collagen type I) and inorganic components (60%- mainly calcium hydroxyapatite). The arrangements of these components gives bone its anisotropic mechanical properties (B. Zhang et al., 2020). In contrast to cartilage, subchondral bone consists of a highly calcified ECM comprising primarily Collagen type I. Collagen type I fibrils and their association with inorganic components, namely hydroxyapatite (HAp, $Ca_{10}(PO_4)_6(OH)_2$), in a specific hierarchical structure, confer subchondral bone with its hardness, shock absorption, and ability to transmit mechanical loads. In fact, subchondral bone attenuates 30% of the joint load, while cartilage attenuates only 1-3% (Madry et al., 2010).

The bone ECM encapsulates osteocytes, osteoblasts, osteoclasts, blood vessels, and nerves. Osteoblasts are responsible for forming new bone, while osteoclasts oversee bone resorption. The balance between osteoblastic and osteoclastic activity can be shifted in response to external stimuli. For instance, through mechanotransduction, under load bearing conditions, osteoblastic activity may be enhanced. On the other hand, bone resorption may be increased under certain metabolic conditions when more calcium or phosphorous ions are required. After fulfilling their role of bone ECM synthesis, osteoblasts either undergo apoptosis (80%) or terminal differentiation into osteocytes (20%) (Ginebra et al., 2018). Osteocytes are the most common type of cell in bone tissue and regulate both bone formation and resorption (B. Zhang et al., 2020). Figure 4 indicates the osteoblastic differentiation of mesenchymal stem cells (MSCs) and the molecular markers at each stage (Tang et al., 2018). These molecular markers are commonly used to predict and compare the osteogenic potential of various materials.

Anatomically, subchondral bone consists of cortical and cancellous (or trabecular) bone. Cortical bone lies below the calcified cartilage and has limited porosity and limited blood vessels. Trabecular bone, also known as subarticular spongiosa, is characterized by a higher porosity and metabolic activity than

cortical bone. As the porosity increases from the cortical to trabecular bone, the stiffness decreases. The subarticular spongiosa contains MSCs which are multipotent cells of the bone marrow. Subchondral bone also contains nerve fibres and blood vessels. Canals and ampullae extend from the bone marrow into the cartilage across the subchondral bone plate (cortical bone). Perfusion of blood through these canals and ampullae accounts for 50% of the nutritive (glucose, oxygen, water) requirements of cartilage. The remaining nutrition to the cartilage comes from biomechanical movement of the synovial fluid into the tissue. When there is an osteochondral defect, MSCs can migrate through these canals into the cartilage, where they can differentiate into chondrocytes or osteocytes (Farr & Gomoll, 2018). Table 1 from an article by Zhang et al. summarizes the biochemical, structural and mechanical properties of the components of the osteochondral unit (B. Zhang et al., 2020).
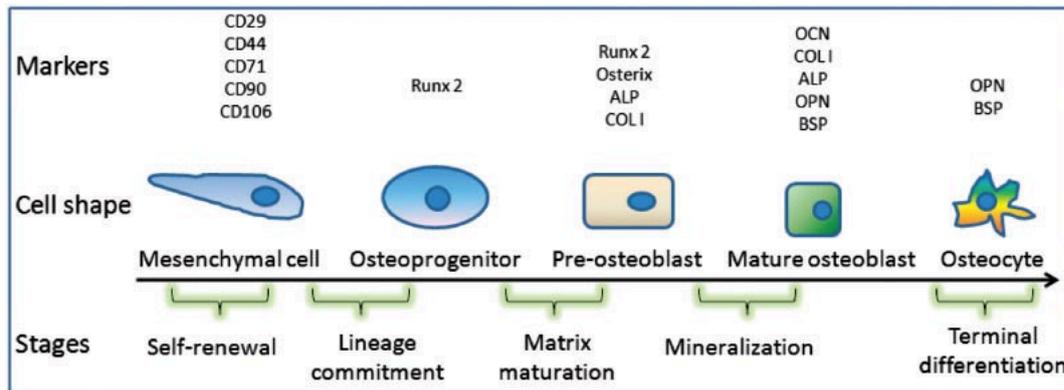

Figure 4: Osteoblastic differentiation of MSCs and the molecular markers at each stage (Tang et al., 2018)

Table 1: Biochemical, structural and mechanical properties of cartilage, calcified cartilage and sub-chondral bone (B. Zhang et al., 2020)

Table 1   The gradient biochemical composition, structure, and mechanical properties of OC natural tissue

	Biochemical composition		Structure	Mechanical properties
	Cells	Materials		
Cartilage[15,26,41,42]	Chondrocyte morphology is flattened in the cartilage surface zone and gradually becomes round and ellipsoid in shape in the deep zone	Type II collagen fibrils are parallel to the joint surface in the cartilage surface zone and gradually become perpendicular to the joint surface in the deep zone	Cartilage is a highly interconnected tissue with a porosity of 60–85% and a pore size of 2–6 nm	The compressive modulus of cartilage increases from the superficial to the deep zone from 0.2 to 6.44 MPa
Calcified cartilage[43–45]	Chondrocyte size in calcified cartilage is higher than in cartilage	Collagen fibrils are anchored to the subchondral bone and hold the cartilage and subchondral bone	Calcified cartilage is located in the transition zone from cartilage and bone; its pore size and porosity gradually vary	The compressive modulus values of cartilage, calcified cartilage, and bone exhibit anisotropic properties and vary in a depth-dependent manner
Subchondral bone[46–50]	Osteoblasts, osteoclasts, osteocytes, and MSCs	Hydroxyapatite crystalline plate-shaped particles with a length of 20–50 nm, a width of 15 nm, and a thickness of 2–5 nm are deposited on type I collagen fibrils	Subchondral bone contains cortical bone (top) and trabecular bone (bottom). The pore size varies from 0.1 to 2000 μm and the porosity changes from 5 to 90% from the top to the bottom of the subchondral bone	Compressive modulus values for cortical bone and trabecular bone are 18–22 GPa and 0.1–0.9 GPa, respectively

1.2. Osteoarthritis

Osteochondral lesions, as the name suggests, are defects involving both the cartilage and underlying subchondral bone. These can be caused due to trauma or aging, or in some cases genetic diseases such as osteochondritis dissecans. If left untreated, osteochondral defects can lead to degrative diseases such as osteoarthritis. Osteoarthritis is a common joint disease in elderly patients, and results in chronic disability. It has been estimated by the WHO that 25% of patients suffering from osteoarthritis have trouble performing daily activities and 80% have limited mobility (B. Zhang et al., 2020). It is estimated that knee osteoarthritis affects 654 million people worldwide (Cui et al., 2020). With the ageing and increasingly obese population, this number is projected to increase. The medical costs of osteoarthritis treatment in high income countries accounts for 1-2.5% of the national GDP (Hunter & Bierma-Zeinstra, 2019). Evidently, this represents a substantial burden for healthcare systems.

Although it was previously thought that destruction of cartilage is the hallmark of osteoarthritis, osteoarthritis is a disease of the entire joint capsule (Goldring & Goldring, 2016; Wei & Dai, 2021). Structural alterations to all the synovial joint tissues are observed, including articular cartilage, subchondral bone, ligaments, menisci, joint capsule, and synovium. The etiology of OA involves mechanical, inflammatory, and metabolic factors which eventually lead to destruction and failure of the whole knee joint. OA arises from an imbalance between catabolic and anabolic processes of the joint tissue (Hunter & Bierma-Zeinstra, 2019).

Since subchondral bone is highly innervated and cartilage is not, subchondral bone involvement in OA is likely one of the main contributors to pain in this disease (Wei & Dai, 2021). Microstructural and histopathological changes to the subchondral bone in the pathogenesis of osteoarthritis are receiving more attention recently. The physical linkage between cartilage and bone in the osteochondral junction is impaired during the pathogenesis and progression of osteoarthritis. This impairment includes changes such as microcracks in cartilage and bone, duplication of the tidemark, in growth of blood vessels and nerves from the bone into the cartilage. This leads to an increase in the movement of signaling molecules, growth factors and cytokines from bone to cartilage (Lin et al., 2014). Using treatment strategies which only focus on cartilage repair fail to repair the entirety of the damaged tissue, and therefore are not sufficient to manage or treat osteoarthritis.

1.3. Conventional repair strategies for osteochondral lesions

There is a discrepancy between the intrinsic healing capacities of cartilage and subchondral bone, which stems from the fact that cartilage is not vascularized, while bone is vascularized. Due to the low cell density of chondrocytes and their low proliferative capacity, as well as the avascular nature of AC, articular cartilage is virtually unable to self-heal from degeneration (Camarero-Espinosa et al., 2016; Kwon et al., 2019). As such, surgical treatments are needed to reduce pain, repair damaged tissue and restore joint mobility. The type of surgical treatment indicated depends on the severity of symptoms, size and severity of the lesion (guided by the ICRS or Outerbridge classification) and patients' overall health status (Farr & Gomoll, 2018; Zhou et al., 2020).

The main treatments used in clinical practice include autologous chondrocyte implantation (ACI), matrix-induced autologous chondrocyte implantation (MACI), microfracture, autografts and allografts. ACI and MACI are surgical techniques which harvest a patient's own chondrocytes, followed by expansion on a matrix, and implantation into the lesion. The main limitation is the formation of fibrocartilage with type I collagen predominantly, and poor durability. Further they are incapable of repairing an osteochondral lesion which involves the subchondral bone. Microfracture is used for repairing full thickness (but smaller than 1 cm^2) osteochondral defects. In this technique, holes are drilled into the cartilage and subchondral bone, which stimulates the flow of blood and bone marrow. MSCs and other biomolecules can induce the formation of osteochondral tissue, however the fibrocartilage formed lacks sufficient biomechanical properties. Additionally, this regeneration capacity is limited to small sized defects (Camarero-Espinosa et al., 2016).

Allografts can provide the flexibility to repair larger defects (1-4 cm^2). However, they can result in immune rejection, poor integration with host tissue, possibility of disease spread and low cell viability from long term graft storage (Camarero-Espinosa et al., 2016; Kimber & Shelton, 2010). In severe cases, total joint replacement with a metallic prosthesis is performed. Total joint replacement is an invasive end-stage intervention. In addition, the implants wear out over time and revision surgery is limited (Fortin et al., 2002). It is clear that current surgical therapies do not provide long-term solutions for cartilage regeneration. Tissue engineering strategies represent a promising alternative (Yang et al., 2017). Figure 5 from an article by Wei and Dai depicts the progress in treatment of osteochondral lesions over the last 80 years (Wei & Dai, 2021).
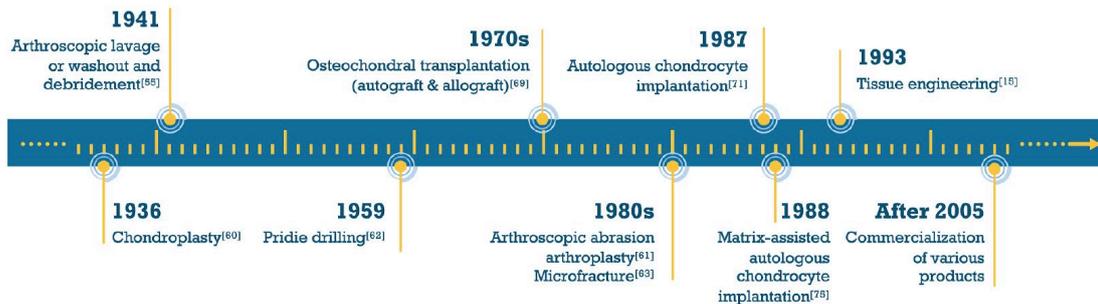
Figure 5: Progress in the treatment of osteochondral lesions (Wei & Dai, 2021)

1.4. Tissue Engineering strategies

Most studies report that the compressive and shear modulus of tissue engineering cartilage are still inferior to native cartilage (Lepage et al., 2019). The biomechanical properties of the osteochondral unit are intrinsically tied to its zonal anisotropic structure. Tissue engineering offers the possibility to repair osteochondral lesions by using cell laden or cell free scaffolds. Scaffolds are 3D constructs which are temporarily used to fill an osteochondral defect and provide the right microenvironment to produce complex and zonally organized tissue. An ideal osteochondral scaffold must be biocompatible, have mechanical properties approaching that of the host tissue, as well as appropriate pore size and porosity (Wei & Dai, 2021). Pore size and porosity play an important role in chondrogenesis and osteogenesis. A scaffold with a pore size of over 300 µm and porosity of over 50% is conducive to osteogenesis, whereas a pore size of 90-120 µm is more favorable for chondrogenesis. Native cartilage has a pore size of 6 nm on average, calcified cartilage has a porosity of around 22% and subchondral bone has a porosity of 64-94% (Doyle et al., 2021). Studies show that when pore size and porosity are higher, there is an increase in cell migration, proliferation, and exchange of nutrients and metabolic waste. On the other hand, a higher porosity usually results in lower mechanical strength. It is critical to consider this delicate balance between pore size, porosity, pore interconnectivity along with the mechanical and cell behavior. In addition, the scaffold should degrade at the same rate at which new tissue is formed. This delicate balance between porosity, biomechanical properties and degradation behavior can be effectuated through the appropriate choice of **biomaterials, cell types, scaffold architectures, biochemical/ physiochemical or physical signaling factors and fabrication techniques** used to create the scaffold (Wei & Dai, 2021; B. Zhang et al., 2020). All of these factors are codependent i.e. when selecting a material, the fabrication process must be taken into account and vice versa. These scaffold considerations are discussed in the below sections.

1.4.1   Biomaterials for osteochondral tissue engineering

A wide variety of biomaterials have been used for osteochondral tissue engineering, ranging from natural polymers (polysaccharide and protein-based materials, synthetic polymers, bioceramics, metals and decellularized ECM). Polymers in the form of hydrogels have been used extensively in cartilage tissue engineering. Hydrogels are a highly hydrated 3D polymeric network, with a favorable environment for cells, similar to native ECM (Yang et al., 2017).

1.4.1.1. Natural polymers

Natural polymers such as hyaluronic acid, chondroitin sulphate, alginate, agarose, chitan, gellan gum, collagen, gelatin and silk fibroin are commonly used due to their structural similarity to proteoglycans of the ECM. Gelatin is a derivative of collagen obtained through its partial hydrolysis. It is biologically active and has a lower immunogenicity than collagen. Further pig, which is usually the source for gelatin hydrogels, has the most similar collagen structure to that of humans (Zhou et al., 2020). The inadequate mechanical properties and rapid degradation of gelatin can be overcome through chemical modification with methacryloyl at the primary amine and hydroxyl groups. GelMA (Gelatin methacryloyl) can be covalently crosslinked under UV through photoinitiated radical polymerization. Covalently crosslinked hydrogels, compared to their physically cross-linked counterparts or non-crosslinked, are much stronger and more stable and thus are preferred for tissue engineering applications. GelMA is a versatile hydrogel and many of its properties can be tailored to the application. The mechanical properties, degradation behavior, swellability and pore size of GelMA can be tailored through adjusting the GelMA polymer concentration, the photoinitiator type and concentration, degree of substitution of methacryloyl groups and UV exposure time. Further, there is spatial and temporal control of the cross-linking process, which this allows for the microfabrication of this hydrogel in unique 3D morphologies (Yang et al., 2017).

In addition, methacrylated gelatin retains its cell friendly environment since chemical modification does not affect the RGD amino acid sequences (arginine-glycine-aspartic acid) or the target sequence for MMPs (matrix metalloproteinases). The RGD amino acid sequence allows for cell attachment, whereas the MMP target sequence allows the enzymatic degradation by matrix metalloproteinases and subsequent cell remodeling. Regardless, hydrogels are limited by their low compressive stiffness, making them largely unsuitable as the sole biomaterial component for a load bearing tissue (Yang et al., 2017; Yue et al., 2016).

1.4.1.2. Synthetic polymers

Scaffolds composed of synthetic polymers such as polycaprolactone (PCL), poly (ethylene glycol) (PEG), polylactic acid (PLA), polyglycolic acid (PGA), poly(lactic acid-co-glycolic acid) (PLGA), , poly(vinyl alcohol) (PVA), poly (propylene fumarate) (PPF), poly(L-glutamic acid), and poly(N-isopropyl acrylamide)(PNIPAAm) have been used in osteochondral tissue engineering. Compared to natural polymers, synthetic polymers offer higher control over their molecular weight and degradation, as well as ease of production on an industrial scale (Wei & Dai, 2021). However, most of these polymers are hydrophobic, which limits their bioactivity since there are an insufficient number of cell interaction sites (Huang et al., 2018). PCL is one of the most used synthetic polymers for bone tissue engineering. This FDA approved thermoplastic polymer is biocompatible and has a degradation rate comparable to bone regeneration i.e. a few months to years. However PCL is not osteogenic due to its structural dissimilarity with bone ECM as well as inferior mechanical strength compared to native bone (Gerdes et al., 2020). Consequently studies have reported using a blend of natural or synthetic polymers with bioceramics for osteochondral TE to stimulate biomineralization and better approximate the mechanical properties of the host tissue (B. Zhang et al., 2020).

1.4.1.3. Bioceramics

For bone tissue engineering, load bearing abilities of the scaffold material are a critical consideration. If the implant strength is much lower than the surrounding bone, the implant will fail before bone growth. On the other hand, if the scaffold material is much stronger such as some metals, stress shielding will protect the bone from normal mechanical loading causing bone resorption (Huang et al., 2018). Bioceramics such as calcium hydroxyapatite, bioglass, calcium silicate and tri-calcium phosphate are the most ubiquitously used materials in bone regeneration. This is because of their resemblance with the inorganic component of bone ECM, good biocompatibility, osteoconductivity and osteoinductivity. Osteoinduction is the ability to induce stem and progenitor cells to differentiate into the osteoblastic lineage and induce ectopic bone formation. Osteoconduction on the other hand refers to bone growth on a surface (B. Zhang et al., 2020). In 1988, Heughebaert was the first to report the formation of a bone like tissue induced by hydroxyapatite implantation in non-osseous sites in hamsters, thus indicating the osteoinductivity of CaP (calcium phosphate) materials (Heughebaert et al., 1988). There are various material characteristics of CaP materials which contribute to their osteoinductivity.

Material characteristics such as phase composition and solubility, Ca^{2+} and PO_4^{3-} ion release, micro and micro pore structure, topographical features, nanoscale and microscale structure and bone-like apatite formation all affect osteoinductivity. The solubility of HA ($Ca_{10}(PO_4)_6(OH)_2$) and β-TCP ($Ca_3(PO4)_2$) both *in vitro* and *in vivo* have been extensively studied. Studies have found that the solubility of calcium phosphates is inversely proportional to the ratio of Ca:P ions. β-TCP has a Ca:P ratio of 1.5, compared to HA's Ca:P ratio of 1.67, indicating that β-TCP is more acidic and consequently more soluble in water (Sheikh et al., 2015; Tang et al., 2018). Highly soluble CaPs which release more Ca^{2+} and PO_4^{3-} ions show a preferential protein adsorption on their surface which in turn results in better osteogenesis. In a 2005 clinical trial, patients with bone tumors underwent curettage or resection, followed by implantation of either HA or highly purified β-TCP in the defect site. In all patients in the β-TCP group, the material was partially absorbed and replaced by new bone, mediated by osteoclasts. In the HA group on the other hand, even though HA was incorporated into the bone, there was no evidence of degradation even 130 months post implantation (Ogose et al., 2005). While HA is slow to degrade, its advantage over β-TCP is its mechanical properties, with a compression strength of 160 MPa.

The porosity, pore size, pore connectivity and even pore shape of CaP scaffolds play important roles in osteogenesis. It is speculated that this range of porosity, pore size and pore channels result in mechanically stable scaffolds, while also enabling the adsorption of low molecular weight proteins such as transforming growth factor β-1 (TGF- β1). Studies have indicated that when a CaP material is

implanted into a defect, the formation of an apatite like layer occurs. The formation of this apatite layer, through nucleation and growth of nanohydroxyapaptite crystals, is correlated to osteoinductive behavior of materials. Lastly, adhesion, proliferation and differentiation of bone forming cells tends to be better when a CaP material is nanostructured, as in native bone (Mohammadi et al., 2021; Tang et al., 2018).

The exact biological mechanisms behind the osteoinductivity of CaP materials, linked to their chemical composition and 3D structure, has still not been completely discerned. Figure 6 indicates a possible mechanism for the osteoinductive behavior of CaP. As can be seen from the figure, the mechanism involves not only the bone system, but also the immune system and vascular system. (1) The first osteoinductive pathway is one in which CaPs directly stimulate osteoblastic differentiation of MSCs. CaPs may stimulate a BMP-2 (Bone Morphogenetic Protein-2) autocrine signaling loop within MSCs, as well as upregulating BMP/Wnt signaling and BMP/ Smad signaling. CaPs cause the expression of BMPs and other signaling molecules, through the release of Ca^{2+} and PO_4^{3-} ions as well as their surface topography, which exert their effect through mechanosensitive pathways. (2) The second pathway involves inflammatory cells and progenitor cells which together recruit osteogenic factors, which in turn trigger the differentiation of MSCs. This can occur by monocytes fusing into macrophages, and macrophages differentiating into osteoclasts through osteoclastogenesis. Osteoclasts may attach to the CaP surface and resorb it, leading to the release Ca^{2+} and PO_4^{3-} ions, which can stimulate osteogenic differentiation and ectopic bone formation by MSCs. In an interplay between the inflammatory and vascular system, under inflammatory conditions, endothelial cells and pericytes may be able to transform into osteoblasts. Reviews by Tang et al. and Xiao et al. shed more light on the osteoinductive mechanisms of CaP materials (Tang et al., 2018; Xiao et al., 2020).
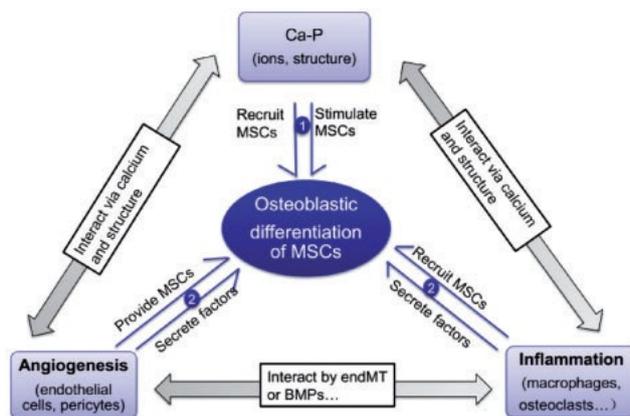

Figure 6: Possible mechanism for osteoinductivity of CaP (Tang et al., 2018)

1.4.2. Scaffold architecture

The past few decades have seen the progress of osteochondral scaffolds from monophasic to biphasic to triphasic/ multiphasic and most recently gradient scaffolds. A monophasic scaffold consists of a homogenous material and structural composition. Clearly this type of architecture fails to recapitulate the structural complexity of osteochondral tissue. Biphasic scaffolds comprise a distinct chondral component and an osteal component. In general, the chondral scaffold is composed of hydrogel composed of a natural or synthetic polymer, which mimics the viscoelastic and hydrated ECM of cartilage and supports the encapsulation and differentiation of various cell types. The osteal component on the other hand usually is made of a bioceramic, metal or stiff polymer (Zhou et al., 2020). In conventional tissue engineering approaches, the osteal and chondral components were simply glued, sutured or press fitted into the suitably prepared osteochondral defect (Diloksumpan et al., 2021). However, there is a risk of phase delamination or dislodgement after implantation. It is still challenging to establish a secure interface between mechanically different material such as a hydrogel and a bioceramic for the osteal component (Diloksumpan et al., 2020).

When considering the attachment of the chondral and osteal components, it is crucial to consider the anatomy of the osteochondral unit. Incorporation of a calcified cartilage layer between the osteal and chondral components can aid in the proper integration of the implant, thereby improving interfacial shear strength and providing a barrier in the diffusion of catabolic factors from bone to cartilage. Therefore, a triphasic or multiphasic scaffold recapitulating these three layers is a promising option for osteochondral tissue engineering (Kosik-Kozioł et al., 2019; Lepage et al., 2019; St-Pierre et al., 2012). However even with a triphasic osteochondral scaffold, incomplete integration of the implant with the host tissue can

result in implant failure. As was seen in a study done by Diloksumpan et al., synovial fluid flowed into the space between the implant and host bone, resulting in osteolysis and limited new tissue deposition (Diloksumpan et al., 2021).

1.4.3. Cell type

While cell-free scaffolds have been used for osteochondral tissue engineering, tissue deposition can be enhanced through the use of cells which can adhere, proliferate, and differentiate into osteogenic and/or chondrogenic lineages. Cell populations residing in the osteochondral unit include chondrocytes, articular chondrocyte progenitor cells, osteoblasts, stem cells with pluripotency or multipotency such as bone marrow mesenchymal stem cells (BMSCs), adipose stem cells (ASCs), embryonic stem cells (ESCs), and induced pluripotent stem cells (iPSCs). Consistent with their anatomical presence, chondrocytes are commonly used for cartilage repair while osteoblasts are used for bone regeneration. The use of terminally differentiated cells has limitations, since the cells need to be harvested, isolated, expanded in vitro, seeded into a scaffold, followed by culture of the cell-seeded scaffold and implantation. Chondrocytes suffer from poor isolation efficiency, proliferation in culture and dedifferentiation when expanded in monolayers. Since chondrocytes and osteoblasts both originate from bone marrow stem cells, MSCs are commonly used for osteochondral tissue engineering. MSCs are relatively easy to isolate and proliferate, can differentiate into chondrogenic and osteogenic lineages, and are not immunogenic (Wei & Dai, 2021). Some studies indicate that articular cartilage progenitor cells (ACPCs) may be more suitable for cartilage tissue engineering than MSCs (Mancini et al., 2020).

Biochemical signaling factors, physical factors and physiochemical factors can play important roles in influencing biological processes and the type of neo-tissue produced by the cells. Commonly used growth factors in bone and cartilage repair are transforming growth factor (TGF)-β, bone morphogenetic proteins (BMPs), insulin growth factors (IGFs) and fibroblast growth factors (FGFs). Physiochemical cues include oxygen tension, pH and carbon dioxide concentration, while physical cues include temperature and mechanical stimuli. Some mechanical stimuli can be transmitted through the fluid tissue components such as hydrostatic shear stress, while other mechanical stimuli can be transmitted through the solid tissue component such as compression and shear. The use of bioreactors is a common strategy to provide cells with the appropriate biomechanical cues and culture conditions (Wei & Dai, 2021; B. Zhang et al., 2020).

1.4.4. Fabrication methods: conventional and 3D printing

There are two main techniques used to fabricate osteochondral tissue scaffolds: conventional techniques and 3D printing. Conventional fabrication techniques such as solvent casting, gas foaming, freeze-drying, and electrospinning, are generally cost effective, but offer limited control over scaffold porosity, pore size and geometry (Wei & Dai, 2021). 3D printing is an additive manufacturing technology that allows for the layer-by-layer deposition of a bioink or biomaterial ink, comprising of biomaterials, and/or cells and growth factors, into a biomimetic structure. The layer-by-layer design is guided by a computer aided design model (CAD) model. 3D printing offers excellent control over pore size and pore connectivity. In addition, biofabrication techniques boast of a higher RTM (spatial resolution: time for manufacturing) ratio than conventional fabrication strategies. This means that large, centimeter sized objects can be created with microscale resolutions in a relatively short printing time (Moroni et al., 2018). 3D printing techniques also allow for the production of complex and irregular geometries matching the osteochondral defect, by using medical imaging such as CTs and MRIs. It is important to note that it is not necessary to mimic a living tissue down to its last detail, but rather create a printed niche which is mechanically competent and contains the necessary cues for cells to deposit neo tissue (Schwab et al., 2020). Commonly used 3D printing techniques used for osteochondral tissue engineering are inkjet-based bioprinting, extrusion-based bioprinting, laser-assisted bioprinting, stereolithography bioprinting and electrohydrodynamic-based printing (Zhou et al., 2020).

The principle behind extrusion bioprinting is similar to that of fused deposition modeling (FDM), in which a molten polymer is extruded through a nozzle and deposited in a layer-by-layer fashion. In extrusion bioprinting, a soft material is loaded into a cartridge and extruded through a nozzle through either mechanical (through a piston or screw) or pneumatic means. The printing resolution is dictated by the bioink's physical parameters such as yield stress, extrusion pressure and nozzle diameter. While in theory a resolution of 5 to 100 µm can be obtained, when cells are incorporated into the bioink, shear stresses must be minimized to avoid damaging the cells. Since shear stresses are inversely correlated

to the nozzle diameter, the actual printing resolution that can be achieved is usually in the range of several hundred micrometers to millimeters. Biomaterial inks (cell free), on the other hand, can be extruded through thinner nozzles with a higher pressure (Schwab et al., 2020). The advantages of extrusion bioprinting include its relatively low cost, availability of a range of commercial printers and inks, multi-material printing using several nozzles, and good cell viability. The disadvantage on the other hand is the time taken to print a large construct (Cooke & Rosenzweig, 2021).

In extrusion bioprinting, filaments are the building blocks and filaments can undergo deformations during the printing process. Gravity can cause collapse or sagging of the filaments, whereas surface tension causes filaments to form shapes that reduce their surface area, leading to fusion of adjacent filaments. Shape fidelity was usually evaluated by visual examination of the filaments or a macro/microscopic evaluation of the printed structure. Shape fidelity refers to how closely a printed structure matches the CAD design. Ribeiro et al. was the first to propose a quantitative test of bioink shape fidelity to enable a reproducible comparison between different bioinks or different concentrations of the same bioink. The first test is a filament collapse test which assesses the angle of deflection of an extruded filament. The filament fusion test on the other hand tests the resolution by examination of pore closure and fusion of parallelly printed filaments. Together these two tests allow for the quantitative evaluation of shape fidelity both in the z axis and the x-y plane (Ribeiro et al., 2018).

As mentioned previously, a blend of a bioceramic and thermoplast is commonly used for bone tissue engineering. PCL is the most ubiquitously used thermoplastic polymer, while HA and β-TCP are the most used bioceramics. Several studies have reported the use of PCL-HA scaffolds (Bittner et al., 2019; Gerdes et al., 2020; Kim et al., 2017; Nyberg et al., 2017). Recently studies have also been performed using PCL- β-TCP for bone tissue engineering (Konopnicki et al., 2015; Nyberg et al., 2017; Park et al., 2016; Wang et al., 2021). The Bittner et al., Gerdes et al., Nyberg et al., as well as the Park et al. study used hot melt FDM. Kim et al. employed the use of NIPS (non-solvent induced phase separation) based 3D plotting. On the other hand, Wang et al. used hot melt FDM in combination with MEW, and Konopnicki et al. used binder jetting. The disadvantage of using high temperatures for the fabrication of scaffolds is that this excludes the possibility to directly incorporate cells and biological factors before printing. Hot melt FDM also poses the disadvantage of polymer masking wherein the thermoplast encapsulates the ceramic particles and inhibits the release and osteogenic activity of ceramic ions. In addition, hot melt fibres are accompanied by slow extrusion rates of 0.5 mm/s to 5 mm/s (Jakus et al., 2016). A study by Jakus et al. was the first to use to solvent-based extrusion printing to fabricate HA-PCL scaffolds (Jakus et al., 2016). The printing process was performed at room temperature, thereby avoiding the disadvantages associated with heating the bioink. The bioink was prepared using a novel tri-solvent mixture comprising dichloromethane (DCM), 2-butoxyethanol (2-Bu) and dibutyl phthalate (DBP). When using a 3 solvent mixture, the presence of 2-Bu and DBP with a lower volatility than DCM, allows the thermoplast to slowly precipitate and coat HA particles. This results in a microstructure with robust particle bridges. Since the mixture does not dry immediately after extrusion, the ink also acts as a self-adhesive allowing the stacking of fibres and layers into a multilayered 3D structure (Jakus et al., 2016). The study found that the HA (90% weight)-PCL (10% weight) scaffolds had elastic mechanical properties, supported cell proliferation and differentiation of MSCs into an osteogenic lineage, without the use of osteogenic growth factors in the culture media. To our knowledge, solvent-based extrusion printing has not been used to fabricate PCL- β-TCP scaffolds.

Another commonly used fabrication technology for cartilage tissue engineering is melt electrowriting (MEW). MEW is a fabrication technique that can allows for the deposition fibres with a micro or nanoscale diameter. Since collagen fibrils in articular cartilage have a diameter of 100-300 nm, it is evident that MEW allows for the fabrication of ECM mimetic scaffolds with the structural competency. The working principle of MEW consists of the application of an electric field which draws out a molten polymer out of a spinneret towards a moving collector plate. By moving the collector plate at a speed close to that of the polymer jet, accurate fibre deposition and stacking can be achieved, which further allows the creation of complex scaffold architectures (Daghrery et al., 2022).

Recent studies have investigated using soft cell-laden hydrogels reinforced with a micro-fibre scaffold obtained by direct melt electrospinning (MEW) (Castilho et al., 2018; Castilho, Mouser, Chen, Malda, & Ito, 2019; de Ruijter, Ribeiro, Dokter, Castilho, & Malda, 2019; Visser et al., 2015). The load bearing abilities of hydrogels are significantly improved through the reinforcement with a fibrous mesh. Upon compression, the lateral displacement of the hydrogels is resisted by tensioning of the microfibres. This mechanism is reminiscent of the interaction of GAGs and collagen fibrils which renders cartilage its load

bearing ability (Daghrery et al., 2022). However, these studies focus only on cartilage, not on the repair of osteochondral defects.

As described previously, triphasic scaffolds incorporating calcified cartilage layer have advantages over biphasic scaffolds. Namely the inclusion of a calcified cartilage layer aid in the proper integration of the implant, thereby improving interfacial shear strength and providing a barrier in the diffusion of catabolic factors from bone to cartilage. Relatively few studies have focused on engineering the calcified cartilage layer. A study by Diloksumpan et al. in 2020 focused on the integration of a soft hydrogel with a tough bone scaffold through a combination of MEW and extrusion-based printing. The chondral component was composed of GelMA reinforced with a MEW mesh, the interface layer was composed of the MEW mesh and PCaP (comprising nano-hydroxyapatite, α-tricalcium phosphate, and a crosslinkable polyoxamer) and the bone compartment of PCaP. The interlocking design due to the MEW meshes improved hydrogel adhesion strength by over 6.5 fold compared to MEW meshes that were not anchored in the ceramic phase (Diloksumpan et al., 2020). A study by Kosik-Koziol et al. reported the use of a calcified cartilage zone scaffold made of alginate and GelMA, combined with β-TCP microparticles. Scaffolds were fabricated using extrusion-based printing with a coaxial needle system and encapsulated bone marrow MSCs. The authors found that 0.5% w/v is the optimal concentration of β-TCP to obtain scaffolds with the appropriate shape fidelity and markers related to the formation of calcified cartilage (Kosik-Koziol et al., 2019). Liu et al. developed a trilayered scaffold based on GelMA/ nHA (nano-hydroxyapatite) using a multi-nozzle extrusion-based printing system. The trilayered scaffold showed appropriate physical properties (swelling ratio, degradation profile, porosity), mechanical properties (tensile, compressive and interfacial strength) and biocompatibility (cell viability and proliferation). Notably, neo-tissue formation was observed after 12 weeks post implantation in a rabbit osteochondral defect, with good integration with the surrounding tissue and the formation of a tidemark layer (Liu et al., 2019).

1.5. Hypothesis and goals of the present study

The osteochondral unit consists of articular cartilage, calcified cartilage and subchondral bone. The impressive biomechanical properties of osteochondral tissue arise from its unique anisotropic extracellular matrix structure and cell distribution (Goldring & Goldring, 2016). Osteochondral lesions, if left untreated, can lead to a degenerative disease called osteoarthritis. Knee osteoarthritis currently affects 654 million people worldwide and causes chronic pain in affected individuals (Cui et al., 2020). Osteoarthritis also presents a significant burden to healthcare systems. Traditional surgical treatments of osteoarthritis such as microfracture, matrix-induced autologous chondrocyte implantation (MACI) and allografts, have limited efficacy and often lead to the formation of mechanically inferior fibrocartilage. Tissue engineering strategies represent a promising alternative for the regeneration of osteochondral tissue (Camarero-Espinosa et al., 2016). Many factors must be considered when designing a tissue engineering scaffold. These include the appropriate choice of biomaterials, scaffold architecture, cell types, and fabrication technology (Wei & Dai, 2021). Historically, biphasic scaffolds have been widely used, comprising of a hydrogel phase for the chondral tissue and a bioceramic phase for the osteal tissue. These scaffold architectures usually fail due to phase delamination and dislodgement of the construct (Diloksumpan et al., 2020). The importance of the calcified cartilage layer in providing a secure mechanically competent interface between cartilage and bone cannot be understated. Relatively few studies have focused on engineering calcified cartilage tissue.

The blend consisting of a bioceramic and a thermoplastic polymer are commonly used for bone tissue engineering, mitigating the brittleness of bioceramics and poor mechanical strength of thermoplasts. HA and β-TCP are commonly used due to their osteogenic properties. While HA is mechanically stronger, β-TCP is a more soluble bioceramic and might simulate both chondrocyte hypertrophy and osteogenesis faster than HA (Gerdes et al., 2020; B. Zhang et al., 2020). Jakus et al. reported using a solvent-based extrusion printing at room temperature to fabricate HA-PCL scaffolds (Jakus et al., 2016). However to our knowledge, solvent based extrusion has not been previously used to fabricate β-TCP-PCL scaffolds. In the present study we present a novel β-TCP-PCL biomaterial ink and compare it to the established HA-PCL biomaterial ink to assess their potential for engineering the calcified cartilage tissue. The difference between our study and that of Jakus et al. is that we use nanoparticles of HA and β-TCP since adhesion, differentiation and proliferation of cells tends to be better when the material is nano structured as in native cartilage and bone (Tang et al., 2018). The hypothesis is that scaffolds composed of β-TCP- PCL will release more osteogenic ions and lead to the fast deposition of calcified cartilage tissue through chondrocyte hypertrophy.

A comparative study between two biomaterial inks, HA-PCL and β-TCP- PCL, will be performed comparing their 1. printability and shape fidelity, 2. ability to form porous scaffolds, 3. degradation profiles, and 4. biological performance. Figure 7 shows a schematic of the current study.

1. Solvent based extrusion printing at room temperature has not been used previously to fabricate a β-TCP-PCL scaffold. Therefore, we investigate whether a β-TCP-PCL biomaterial ink can be synthesized and processed in the same way as the already established HA-PCL biomaterial ink, using solvent-based extrusion printing. Shape fidelity of the biomaterial inks of various concentrations will be compared through a filament collapse test and a filament fusion test. One concentration of the HA biomaterial ink and β-TCP biomaterial ink respectively with the best shape fidelity will be used for the rest of the study.

2. The ability of the β-TCP-PCL biomaterial ink to form porous scaffolds, as compared to the established HA-PCL biomaterial ink will be assessed.

3. A degradation study will be performed to assess the degradation profiles of these two bioceramics under enzymatic and non-enzymatic conditions, analyzing the release of calcium and phosphorous ions.

4. An *in vitro* study will be performed over 28 days to compare the biological performance and neo-tissue deposition of calcified cartilage scaffolds composed of these two materials. Here the chondrocytes will be seeded directly onto ceramic dics or encapsulated in a hydrogel which is placed in close contact with the ceramic disc. The hypothesis is that cells seeded directly onto ceramic discs feel the effect of the calcium and phosphorous ions more intensely than GelMA since ions have to diffuse into the media and through the hydrogel to reach the cells.

Figure 7: Schematic illustrating the research question and experimental set-up, created using biorender.com. Schematic of the osteochondral unit obtained from an article by Madry et al. (Madry et al., 2010), solvent based extrusion printing figure obtained from an article by Zhang et al.(Zhang et al., 2021), printability schematic obtained from Golafshan et al. (Golafshan et al., 2020), Mass spectrometer image obtained from https://www.medicalexpo.com/prod/perkinelmer/product-69673-851286.html

2. METHODS

2.1. Preparation of biomaterial inks

The first set of pastes for extrusion printing were prepared by combining nano-hydroxyapatite (HA) (Sigma-Aldrich, Germany) and commercial medical grade Poly (ε-caprolactone) (Purasorb PC 12, Purac biomaterials, Netherlands) in different volume ratios (70% HA-30% PCL, 60% HA-40% PCL and 50% HA- 50% PCL). The second set of pastes for extrusion printing were prepared by combining milled and nano-sized β- tricalcium phosphate (β-TCP) and medical grade Poly (ε-caprolactone) (Purasorb PC 12, Purac biomaterials, Netherlands) in different volume ratios (70% β-TCP-30% PCL, 60% β-TCP -40% PCL and 50% β-TCP- 50% PCL). The powders were dissolved in a high volatile 3 solvent mixture consisting of dichloromethane (Sigma-Aldrich, Germany), 2-butoxyethanol (Merck, Germany) and dibutyl phthalate (Sigma-Aldrich, Germany) in a ratio of 10:2:1 v%. The exact compositions for each mixture are presented in Table 2. The ceramic and thermoplast ratios as well as the solvent composition were chosen based on previous literature article (Golafshan et al., 2020; Jakus et al., 2016). Each paste was mixed with a clean metal spatula and left to homogenize on a roller mixer for 7 days at room temperature. Prior to extrusion printing, the pastes were mixed using a spatula to evaporate the excess solvent and obtain the optimal viscosity for printing. Pastes were manually stirred under the fume hood for two minutes at a time, at five-minute intervals for five hours a day, over 2-3 days. Due to the toxic and volatile nature of the solvents, a glass pipette was used, and these pastes were prepared under the fume hood.

Table 2: Composition of ceramic pastes

	Weight of ceramic component (g)	Weight of PCL (g)	Volume of 3 solvent mixture (ml)
70% HA-30% PCL	4.6	5.6	20
60% HA-40% PCL	3.4	6.8	20
50% HA- 50% PCL	2.3	7.92	20
70% β-TCP-30% PCL	6.2	5.6	20
60% β-TCP-40% PCL	5.6	5.6	20
50% β-TCP- 50% PCL	4.4	5.6	20

2.2. Printability tests

Printability of the different pastes was assessed by a filament collapse test and filament fusion test. These printability tests were performed following the protocol described by Ribeiro et al. (Ribeiro et al., 2018). The piston driven extrusion-based printing system 3D discovery (RegenHU, Switzerland) was used for scaffold fabrication as well as printability tests. First, pastes were transferred to a 10 ml syringe (Nordson EFD, USA) and extruded using a 22 G nozzle, with an inner diameter of 0.41 mm (Nordson EFD, USA). To dispense the paste, the extrusion pressure was 0.120 MPa. However, for each new paste that was extruded from the nozzle, the pressure was optimized according to the pastes' viscosity.

2.2.1. Filament collapse test

A platform with pillars (l*w*h= 2*2*4 mm) spaced 1 mm, 2 mm, 4 mm, 8 mm and 16 mm apart from each other was placed on the stage of the 3D discovery printer (RegenHU, Switzerland). The platform was composed of PIC100 resin and secured onto the stage with tape. The nozzle was positioned 0.3 mm above the first pillar and a single filament was deposited over the pillars using the 3D discovery bioprinter (g-code in supplementary information S2). The deposition speed was 8 mm s^{-1}. The extrusion was stopped after the filament had extended about 20 mm after the last pillar. Next, a photo was obtained with a phone camera and the filament sagging was quantified by measuring the angle of deflection (θ) at the edge of the suspended filament using FIJI software (version 2.1.0/ 1.53 c). All measurements were repeated 3 times and plotted measurements represent an average of 3 measurements.

2.2.2. Filament fusion test

The filament fusion test consisted of printing the pastes in a meandering pattern composed of parallel filament strands, with the spacing increasing spacing every five strands. The pattern started at a filament distance of 0.5 mm, increased 0.5 mm at each subsequent line and ended at 2.5 mm. The pastes were deposited in the above-described pattern (g-code in supplementary information S3) on a glass slide placed on the stage. The deposition speed was 10 mm s^{-1}. Immediately after printing, figures were procured with a stereomicroscope (Olympus SZ61, magnification 4.2x, 2040×1536 pixels). Since the microscope could not capture the entire meandering pattern in a single figure, multiple figures for

each meandering pattern were obtained and merged using Adobe photoshop 2020 software. The fused segment length (fs) at every filament distance (fd) was quantified using FIJI (version 2.1.0/ 1.53 c) and fs was normalized by dividing it by the filament thickness (ft). All measurements were repeated 3 times and plotted measurements represent an average of 3 measurements.

2.3. Preparation of the ceramic discs

To prepare ceramic discs of the desired size, first, a PDMS mould of the same size was fabricated. First a PLA negative mould consisting of cylinders of the desired size were fabricated with Ultimaker Cura. Next, to make the PDMS mould, SYLGARD 184 Silicone Elastomer Base (Dow, Germany) and the cross linker SYLGARD 184 Silicone Elastomer Curing Agent (Dow, Germany) were combined in a 10:1 weight ratio. The mixture was then placed in a desiccator for 10 minutes to get rid of air bubbles. Subsequently, the mixture was poured over the PLA mould and placed in the oven at 60° for one hour. After the PDMS mould had solidified, it was detached from the PLA negative mould. Lastly, to prepare the ceramic discs, ceramic paste (70% HA-30% PCL and 70% β-TCP -30% PCL) was placed into the PDMS mould and the surface was smoothed with a glass slide. The paste solidified in the span of a few hours after which it was easily detached from the PDMS mould, resulting in ceramic discs with the desired dimensions i.e. 3.8 mm diameter and 2.04 mm height.

2.4. Printing porous bone scaffolds

Using 3D discovery (RegenHU, Switzerland), a large rectangular bone scaffold 4 cm long was printed composed of 10 layers with a height of 4 mm. G-code can be found in the supplementary information (S4). Images of the scaffold were obtained with a stereomicroscope (Olympus SZ61) and the filament diameter and pore size of the bone layer were quantified with FIJI (version 2.1.0/ 1.53 c).

2.5. Ion release study from ceramic discs

The release of calcium and phosphorous ions from the ceramic discs were measured over 15 days with Inductively Coupled Plasma- Mass Spectrometry (ICP-MS, Varian, Darmstadt, Germany). Ceramic discs prepared as explained in section 2.3 were placed in either PBS or PBS supplemented with 0.4 mg/ ml lipase at 37°C. At each time point, the media (i.e. PBS or PBS with lipase) was first diluted 10x with 1.3 v/v% 65% nitric acid (Suprapur, Merck, Schwalbach, Germany). Next, ion concentrations were measured against standard solutions of (Merck, Schwalbach, Germany, Calcium: 0.5 ppm and 1 ppm, and Phosphorous: 100 ppm and 500 ppm). The ion concentrations at each time point (in ppb) were reported relative to the ion concentration in the fresh media.

2.6. *In vitro* experiment

2.6.1. *In vitro* cell culture and experimental set-up

First, equine chondrocytes (P0+1) were harvested from an equine equine metacarpophalangeal joints as described previously (Mouser et al., 2017). After harvesting, the equine chondrocytes were expanded in monolayer culture with a seeding density of $1*10^6$ cells per flask over 10 days until 90% confluent. For the expansion of the chondrocytes, a chondrogenic expansion medium consisting of basal media, composed of Dulbecco's Modified Eagle Medium (DMEM), FBS (10%) and penicillin/streptomycin (1%), was used. Next, chondrocytes (P=3) were encapsulated in GelMA at a density of $20 * 10^6$ chondrocytes/ml, as described below.

The experimental set up consisted of four groups. Figure 8 shows an overview of the experimental set-up. Groups 1 and 2 consisted of chondrocytes seeded directly onto a ceramic disc and Groups 3 and 4 consisted of chondrocytes encapsulated in GelMA and placed on a ceramic disc. Following expansion, 80,000 chondrocytes were either seeded directly onto a ceramic disc composed of 70% HA-30%PCL (Group 1) or a ceramic disc composed of 70% β-TCP-30% PCL (Group 2). Groups 3 and 4 consisted of chondrocytes encapsulated in 10% GelMA at a density of $20 * 10^6$ chondrocytes/ml and the cross linked GelMA was placed on a ceramic disc of either 70% HA-30%PCL (Group 3) or 70% β-TCP-30% PCL (Group 4) respectively.

As mentioned above, in Groups 3 and 4, chondrocytes were encapsulated in 10% (wt%) GelMA. The first step was to sterilize the ceramic discs as well as the instruments including tweezers, spatulas, scissors, teflon moulds and glass slides by placing them in 70% ethanol overnight. The ceramic discs were washed with sterile water for a few hours to get rid of the ethanol. Subsequently, ceramic discs

and instruments were dried in a fume hood under UV for one hour. This ensured effective removal of the cytotoxic solvents prior to *in vitro* cell experiments.

Parallelly, sterile GelMA was weighed in a sterile manner and the required amount was dissolved in sterile PBS0. The tube containing GelMA and PBS0 was placed in a water bath at 45°C to dissolve the GelMA. Next a stock solution of the photoinitiator 2% Lithium phenyl-2,4,6-trimethylbenzoylphosphinate (LAP) was prepared. The solution was sterile filtered using a 0.22 μm microfilter. Next, when the chondrocytes were ready to be encapsulated, the required amount of photoinitiator stock solution was added to the polymer solution to achieve a concentration of 0.2% (2 mg/ml) in the final solution. A pellet with the required cell density was resuspended in the solution containing hydrogel and photoinitiator, via a positive dispersion pipette. The hydrogel was cast into Teflon moulds of the dimensions 3.8 mm diameter and 2.04 mm height using a positive dispersion pipette. After gently cleaning the UV oven with 70% ethanol, the hydrogels were cross linked at 365 nm for 15 minutes. The cross-linked cell laden GelMA samples were placed on top of the ceramic discs of the same dimensions such that the bottom surface of the GelMA and top surface of the ceramic discs were in direct contact.

Cell-laden samples of all four group were placed in a 96 well plate and cultured for in osteogenic differentiation media consisting of 96 ml DMEM, 1 ml P/S, 1 ml ASAP, 1 ml ITS+ premix, 2 μL dexamethasone and 10 ng/ml TGF β-1. All 4 groups were cultured for 28 days at 37 °C. Each well consisted of 200 μL of media and media was refreshed twice a week. After day 1, 14 and 28 of *in vitro* culture, samples were taken for biochemical and histological analysis. Table 3 shows the number of samples corresponding to each time point and each type of analysis performed.

Table 3: Experimental set-up: Groups, sample numbers and analyses

|	Cells seeded on the disc						Cells in GelMA placed on a ceramic disc					
	70% HA- 30% PCL			70% β-TCP- 30% PCL			70% HA- 30% PCL			70% β-TCP- 30% PCL		
Day	1	14	28	1	14	28	1	14	28	1	14	28
LIVE/DEAD	3	3	3	3	3	3	3	3	3	3	3	3
Alamar Blue and DMMB/ Picogreen	3	3	3	3	3	3	3	3	3	3	3	3
Safranin-O	1	1	1	1	1	1	1	1	1	1	1	1
IHC Collagen type I	1	1	1	1	1	1	1	1	1	1	1	1
IHC Collagen type II	1	1	1	1	1	1	1	1	1	1	1	1
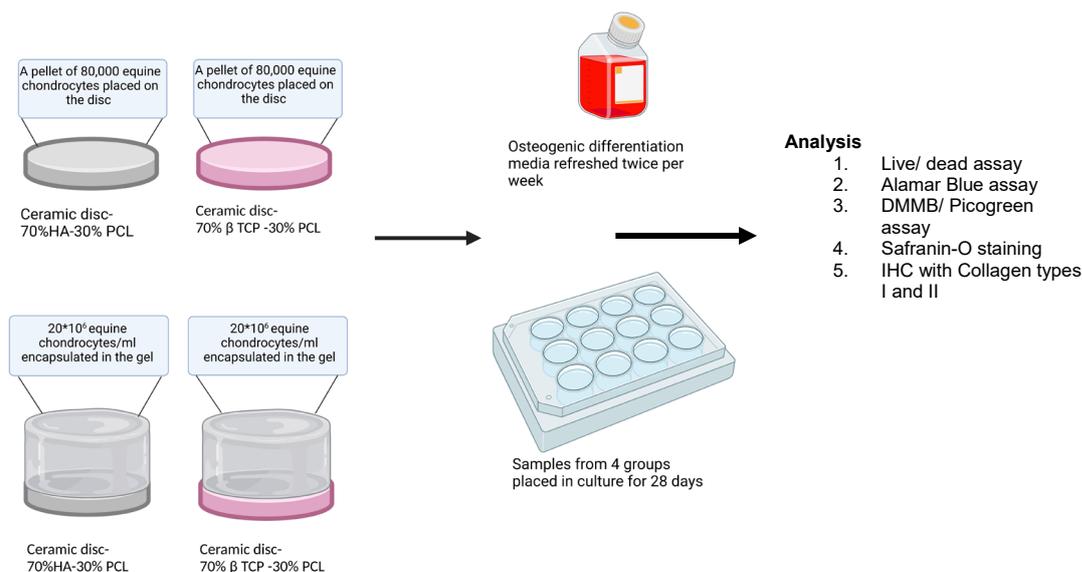
Figure 8: Experimental set-up for the *in vitro* study

2.6.2. Cell viability

Cell viability was determined through a LIVE/ DEAD assay. Calcein-AM stains live cells fluorescent green, indicating intracellular esterase activity and Ethidium Bromide stains dead cells fluorescent red indicating loss of plasma membrane integrity (*LIVE/DEAD™ Viability/Cytotoxicity Kit, for Mammalian Cells*, n.d.). Cell viability was determined at days 1, 14 and 28 using a LIVE/DEAD assay (Ethidium Bromide, Calcein AM, ThermoFisher Scientific). The staining solution was prepared by adding 1 µL of Ethidium Bromide and 0.5 µL of Calcein AM (TermoFischer Scientific) for every ml of PBS. First, media in the wells was aspirated, and the staining solution was added. Next, the well plate was kept covered by aluminum foil for 10 minutes, followed by removing the staining solution and replacing it with PBS. Finally, images were procured with a confocal microscope (Leica SP8 Laser Scanning, Germany). For each sample, three figures were obtained at different locations. FIJI (version 2.1.0/ 1.53 c) was used to calculate the ratio of live cells to the total number of cells, indicating percentage cell viability.

2.6.3. Cell metabolic activity

The Alamar blue dye is a resazurin salt, which is a cell permeable compound that is blue in color and non-fluorescent. Upon entering a cell, the activity of cellular redox enzymes reduces resazurin into resorufin. Resofurin on the other hand is bright red and fluorescent. It diffuses out of cells into culture medium where it can be measured by a fluorometry, thereby providing a quantitative measure of cell viability (Kumar et al., 2018). To measure the metabolic activity of the cells in the samples, Alamar Blue staining (Resazurin sodium salt) was performed at Days 1, 14 and 28. First a 10x stock solution was prepared by dissolving 5.54 mg of Resazurin salt in 50 ml PBS, followed by sterile filtering it and storing it at 4°C. On the day of the experiment, media was aspirated from the wells and the samples were washed 2x in PBS. Next, the stock solution was dissolved 1:10 in DMEM and 300 µL was added to each well. Subsequently the well plate was covered with aluminum foil and incubated at 37°C for 3 hours. After the incubation time, 100 µL of the solution in each sample was pipetted in duplicate into a new 96 well plate. The absorbance values were measured with a fluorescence plate reader, with an excitation wavelength of 544 nm and emission wavelength of 620 nm. Lastly, the leftover Alamar blue solution was aspirated, samples were washed in PBS, osteogenic differentiation media was replenished, and the well plate was returned to the incubator.

2.6.4. Amount of GAGs relative to the DNA amount

After performing Alamar Blue assay on these samples, they were reused for DMMB/ Picogreen. Prior to performing the DMMB and Picogreen assays, the samples were weighed and freeze dried (lyophilized). Both wet weight and dry weight after freeze drying were obtained. Next, they were digested with a papain digestion buffer (0.2 M NaH2PO4, plus 0.01 M EDTA*2H2O in milliQ, pH = 6.0) supplemented with 250 ml/ml papain solution (16–40 units/mg protein, P3125, Sigma Aldrich) and 0.01

M cysteine (C9768, Sigma Aldrich) at 60°C overnight. For the ceramic discs, 20 µL of papain solution was used and for the gel samples, 250 µL of papain solution was used.

The DMMB assay is used to identify glycosaminoglycans. The DMMB reagent (1,9-dimethylmethlene Blue) is a cationic dye which specifically interacts with negatively charged sulphates to produce a colored product. The colored product produces a shift in the maximum absorbance (Barbosa et al., 2003). The DMMB staining solution was prepared by adding 16 mg DMMB (Sigma Aldrich) to 5 ml 100% ethanol. The solution was left to incubate overnight on a rolling plate. After incubation, a sterile filtered solution consisting of 2.37g NaCl and 3.04g Glycine in 1 l distilled water (pH=3.0) was added to the DMMB solution. The staining solution was kept covered by aluminum foil since it is light sensitive.

Next, to prepare a standard curve of Chondroitin sulphate C (0.5 mg/ml), serial dilutions were carried out in PBS-EDTA. The serial dilutions resulted in concentrations of 20 mg/ml, 10 mg/ml, 5 mg/ml, 2.5 mg/ml, 1.25 mg/ml, 0.625 mg/ml, 0.3125 mg/ml, 0.15625 mg/ml, and 0 mg/ml. Subsequently, the papain digested solutions were diluted. The GelMA samples were diluted 1:100, whereas the ceramic disc samples were digested 1:20. Finally, 100 µL of the Chondroitin sulphate standard (in duplicate) and 100 µL of the diluted samples (in duplicate) were pipetted into a 96 well plate. 200 µL DMMB staining solution was added to each well and the absorbance was measured using a microplate reader at 525 nm and 595 nm.

In order to ascertain the amount of GAGs in each sample, first, the 525 nm measurement was divided by the 595 nm measurement. A plot of the Chondroitin sulphate standard curve was made with a polynomic trendline. Next, the polynomic formula $y= ax^2+bx+c$ was used to calculate the amount of GAGs in the diluted samples, where y represents the average absorbance value of the sample, x represents the amount of GAGs in µg/ml, and the values of a, b and c are obtained from the standard curve. Lastly, the value of GAGs in µg/ml was multiplied by the dilution factor to obtain the amount of GAGs in the sample.

The Quant-it Picogreen kit (Thermo Fischer Scientific) was used to determine the DNA content of the samples. First, a standard solution of λDNA (original concentration 100 µg/ml) was prepared by diluting it 50x in Tris-EDTA (TE) buffer to achieve a concentration of 2 µg/ml (2000 ng/ml). To prepare the standards, the λDNA was serially diluted to achieve concentrations of 2000 ng/ml, 1000 ng/ml, 500 ng/ml, 250 ng/ml, 125 ng/ml, 62.5 ng/ml, 31.25 ng/ml, 15.625 ng/ml and 0 ng/ml. The GelMA samples were diluted 100x in TE buffer and the ceramic disc samples were diluted 20x in TE buffer. 100 µL of the λDNA standards (in duplicate) and the 100 µL of the samples (in duplicate) were transferred into a 96 well plate. Next, 100 µL of the PicoGreen reagent (diluted 200x in TE buffer) was added to each well. The 96 well plate was incubated for 5 minutes in the dark. The absorbance values were measured with a fluorescence plate reader, with an excitation wavelength of 480 nm and an emission wavelength of 520 nm. The amount of DNA in each diluted sample was obtained from a linear calibration curve of the λDNA. Lastly, the amount of DNA in each sample (ng/ml) was calculated my multiplying it with the dilution factor. Finally, the amount of GAGs normalized to the DNA amount (in µg/µg) is obtained from this experiment.

2.6.5. Histology and Immunohistochemistry

For histology, the samples (ceramic discs and gels) were fixed in formalin overnight, followed by embedding in liquid paraffin overnight. Next, they were cut into slices 5 µm thick using a microtome, followed by dehydration with a graded ethanol series and clearing with xylene. Sections were stained with Safranin-O to visualize proteoglycans, hematoxylin to visualize cell nuclei, and fast green for collagen. Immunohistochemistry was performed on the samples to visualize collagen types I (primary antibody: rabbit monoclonal antibody ERP 7785, 2.18 µg/ml, abcam) and collagen type II (primary antibody: mouse monoclonal antibody II-II6B3, 2 µg/ml, DSHB). Images were procured using a light microscope (Olympus BX51).

Immunohistochemistry for Collagen types I and II was performed as previously described (Abbadessa et al., 2016). First sections were briefly deparaffinized in xylene and hydrated with ethanol, in decreasing concentrations starting from 100%, until 70%. Next, endogenous peroxidases were blocked with 0.3% v/v H_2O_2 for 10 minutes. Subsequently, antigen retrieval was performed with pronase (1 mg/ml in PBS) for 30 minutes at 37°C, followed by hyaluronidase (10 mg/ml in PBS) for 30 minutes at 37°C. Sections were blocked with 5% PBS/BSA for 30 minutes at room temperature. Following this, sections were

incubated with the primary antibody overnight at 4°C. Mouse IgG was used as a negative control in the same concentration as the primary antibody.

After incubation with the primary antibody, the matching horseradish peroxidase labelled secondary antibody was added. For Collagen type II, Goat Anti Mouse IgG HRP, DAKO P0447 was added and incubated for 60 minutes are room temperature. For Collagen type I, Anti rabbit DAKO envision K4010 was used and incubated for 30 minutes at room temperature. Finally, the staining was developed with DAB (3, 3'-dimaminobenzidine) peroxidase solution and counterstained with Meyer's hematoxylin. After dehydrating and clearing the sections, they were visualized with a light microscope.

2.7.   Statistics
The data is expressed as mean ± standard deviation. The statistical significance between groups was assessed with two-way ANOVA and post hoc Turkey's test (Graphpad prism V8). Differences were considered significant at $p < 0.05$. Different degrees of significance were taken into
account: * for $p < 0.05$, ** for $p < 0.01$, *** for $p < 0.001$ and **** for $p < 0.0001$.

3.   RESULTS AND DISCUSSION

3.1.   Printability tests

3.1.1.   Filament collapse test
Figure 9a depicts the filament collapse test of 3 concentrations of HA-PCL and β-TCP-PCL respectively, as well as plots of the angle of deflection (θ) as a function of the distance from the edge of the pillar to the middle of the suspended filament (L). The filament collapse test gives an indication of the yield stress of the material. Yield stress is the stress below which a material behaves like a solid and above which a material behaves like a liquid (Cooke & Rosenzweig, 2021). In their 2018 article, Ribeiro et al. created a simple theoretical model correlating the yield stress with the angle of deflection of the filament. The final equation is written as

$$\theta = \sin^{-1}(\rho g L / \sigma_{yield})$$

Here ρ is the density of the material, g is acceleration due to gravity which is 9.8 m/s^2 and σ_{yield} is the yield stress of the material (Ribeiro et al., 2018). Yield stress is a critical parameter for a biomaterial ink because a higher yield stress indicates higher shape fidelity. However if the yield stress is too high it is less favorable for cell encapsulation and ECM deposition by encapsulated cells (Mouser et al., 2017).

The first observation from Figure 9a is that as the gap length increases, there is an increase in filament sagging and consequently the angle of deflection. Figure 9a also shows that with an increasing concentration of β-TCP, the angle of deflection decreases. The same trend is observed in the HA based biomaterial ink. For both materials, the angle of deflection in 50% bioceramic-50 PCL > 60% bioceramic-40% PCL > 70% bioceramic- 30% PCL. Evidently the biomaterial inks with the highest bioceramic concentrations i.e. 70% β-TCP -30% PCL and 70% HA-30% PCL have the highest yield stress and the best shape fidelity. A possible explanation is that nanoparticles cause an increase in the viscosity of a material since they impede flow. This is in line with previous studies. A previous study assessed the mechanical properties of a HA-PCL biomaterial ink. Uniaxial tensile tests indicated an increase in compressive yield strength, ultimate tensile strength and elastic moduli with an increase in HA concentration. This was hypothesized to be due to the uniform distribution of stiff HA particles in a more flexible PCL polymer. The stiff HA particles more efficiently retain applied loads (Kim et al., 2017). However, as a follow up to the present study, SEM figures should be obtained to assess the distribution of HA or β-TCP nanoparticles within PCL and to see if they are present on the filament surface or embedded within the depth. A suggestion for future studies is to perform an oscillatory stress sweep to see if the experimental yield stress of the biomaterial inks corroborates the yield stress obtained using the theoretical model of Ribeiro et al. The experimental and theoretical yield stresses should also be compared to that of native calcified cartilage.

3.1.2.   Filament fusion test

Figure 9b shows stereomicroscopy images of the meandering pattern deposited onto the glass slide for three concentrations of HA-PCL and β-TCP-PCL as well as the corresponding plots of fused segment length normalized to filament thickness (fs/ft) as a function of filament distance (fd). For all

concentrations of both biomaterial inks, fs/ ft increases while fd decreases. The graphs suggest a non-linear inverse relation between fs/ ft and fd. Additionally, for all concentrations of both materials, pore closure occurs between 0.5 mm and 1 mm, indicating a similar resolution in the x-y plane for all the biomaterial inks. An observation that is not immediately evident from the stereomicroscope figures is that for both materials, with an increase in bioceramic concentration, the filament thickness increases.

Taking into account the results of the filament collapse and the filament fusion test, the biomaterial inks with the highest ceramic concentrations were chosen for the rest of the experiment. This is because the yield stress is the highest, while resolution is similar, for 70% β-TCP -30% PCL and 70%HA- 30 PCL compared to other concentrations. In addition, the material with the highest ceramic concentration is also hypothesized to display the best osteoinductive behavior *in in vitro* studies.
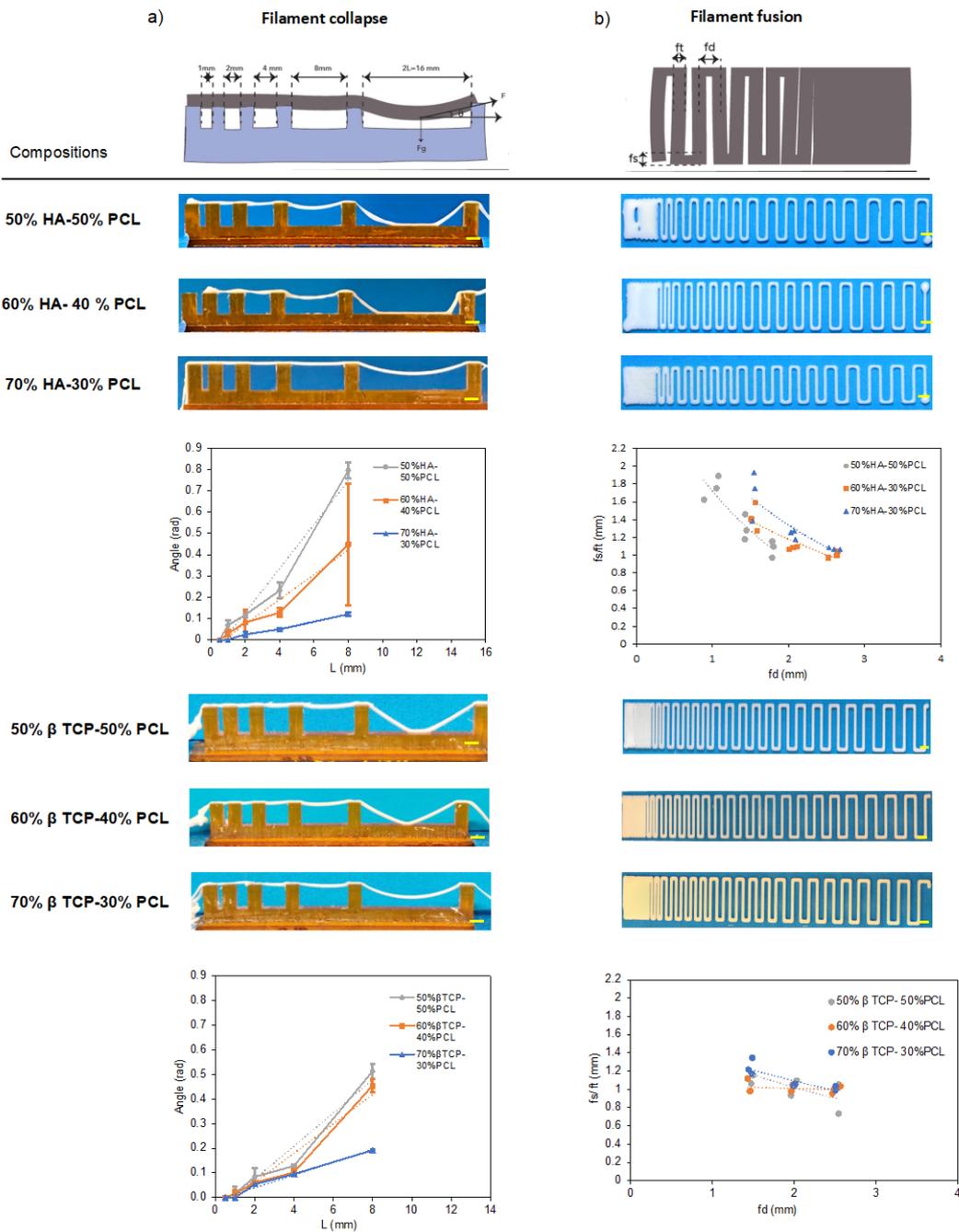
Figure 9: a) Photographs of filament collapse of different concentrations of HA-PCL and β-TCP-PCL and effect of ceramic concentration on the angle of deflection (θ) in radians as a function of half the distance between the pillars (L). Dotted lines indicate a linear regression with the following R^2 values: 70%HA= 0.9925; 60%HA= 0.9615; 50%HA= 0.9622; 50% β-TCP= 0.9532; 60% β-TCP = 0.9404; 70% β-TCP= 0.9833

b) Stereomicroscope images of the filament fusion test and a plot of fused segment length (fs) normalized to filament thickness (ft) as a function of the filament distance (fd), dotted lines represent non-linear regression with exponential fitting. Scale bars in fluorescent yellow in all images indicate 2 mm. The schematics at the top of the image are from an article by Golafshan et al. (Golafshan et al., 2020)

3.2. Pore size and filament diameter of porous HA-PCL and β-TCP-PCL scaffolds

After selecting one concentration of each biomaterial ink, the next step was to assess if these two biomaterial inks can be used to print porous structures. The bone scaffold was fabricated with an extrusion printer and consists of 10 layers with a total height of 4 mm. As seen in Figure 10, the filament diameter of the scaffold composed of 70% HA- 30% PCL is 430 ± 31 μm and the pore size is 549×576 μm. The filament diameter and pore size of the 70% β-TCP- 30% PCL scaffolds on the other hand are 363 ± 23 μm and 466×492 μm respectively. The pore sizes are in the range of 300- 900 μm which is favorable for bone ingrowth.

Pore size and porosity have a high degree of influence on the biological performance of a scaffold. The porous architecture of a scaffold can be categorized into macroporosity (>50 μm) and microporosity (<50 μm). Studies have shown that a pore size of 300 μm and porosity of over 50% is conducive to bone ingrowth and osteogenesis. Pores play a crucial role in the inflow of oxygen and nutrients and the outflow of waste products. In addition, a porous structure allows for better interlocking between the implant and bone and better mechanical stability at the interface. Macroporosity allows for cell ingrowth and proliferation as well as enhanced vascularization. The porosity of trabecular bone is over 90% whereas that of cortical bone is about 20%. Microporosity, on the other hand, results in a larger surface area, which can increase the adsorption of bone forming proteins. Strut thickness and the microporosity of the struts also affect vascularization, and high strut microporosity can promote osteogenesis *in vivo*. Not only pore size and porosity, but pore interconnectivity must also be considered in scaffold design. Studies have shown that a pore interconnectivity of 30%-90% is conducive to vascularization and provides adequate space for bone ingrowth (Mohammadi et al., 2021; Xiao et al., 2020). A suggestion for future studies is to measure the scaffold porosity and interconnectivity using micro-CT. While large pore sizes favor bone ingrowth, the mechanical properties are often compromised. This is because larger pores and a higher porosity lead to faster degradation, which leads to a compromise in the structural integrity of the scaffold before new bone is formed (Mohammadi et al., 2021). The scaffolds fabricated in this study have a pore size conducive to bone ingrowth. However, tensile tests should be performed to examine whether the pore size of the scaffolds in this study compromise the mechanical characteristics such as compressive strength.
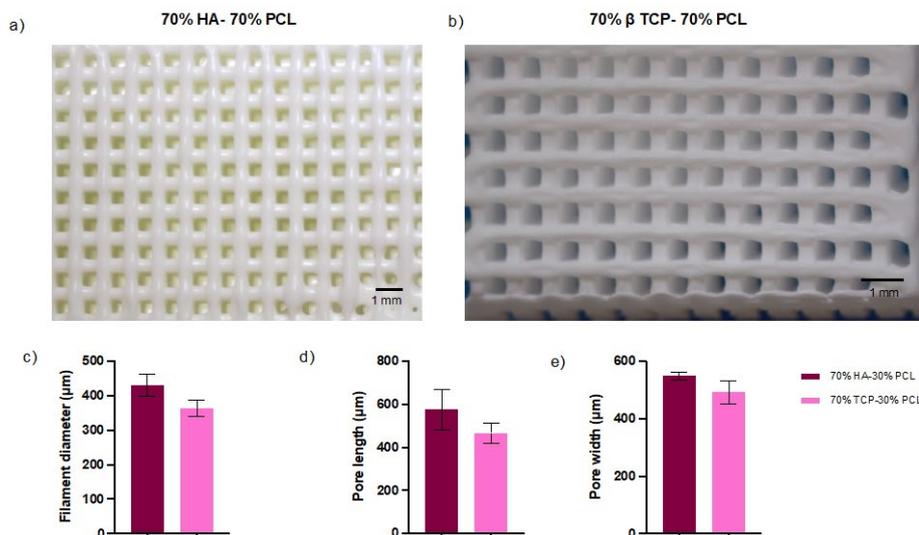

Figure 10: a) Stereomicroscope figure of a bone scaffold composed of 70% HA- 30% PCL. b) Stereomicroscope figure of a bone scaffold composed of 70 β-TCP-30% PCL. Comparison of c) Filament diameters (μm), d) Pore length (μm), and e) Pore width (μm).

3.3. Ion release study from ceramic discs

After having selected one concentration of HA-PCL and β-TCP-PCL each with the best shape fidelity as well as using these materials to print porous scaffolds, we zoom into the calcified cartilage layer. The release of calcium and phosphorous ions from a ceramic disc mimicking the calcified cartilage layer was studied. A challenge associated with combining a bioceramic with a polymer is that sometimes polymers may mask the ceramic phase and hinder the release of osteogenic ceramic ions. Therefore, the degradation behavior of the two materials were investigated (Jakus et al., 2016). As can be seen from Figure 11a, in PBS, the release of both Ca and P ions is higher from the PCL- β-TCP discs, starting from day 5 until day 15. The difference between ion release is more evident under enzymatic conditions, as seen in Figure 11b. A 1.3 x increase in the release of Ca and a 3x increase in the release of P ions can be observed from the PCL- β-TCP group compared to PCL-HA. These results indicate that the ceramic ions are highly exposed, and not being masked by PCL. In addition, as expected, there is a higher release of Ca and P ions from the TCP material, due to the higher solubility of β-TCP. The next step is to investigate whether the higher release of osteogenic ions induces the formation of calcified cartilage tissue.

a) Degradation in PBS
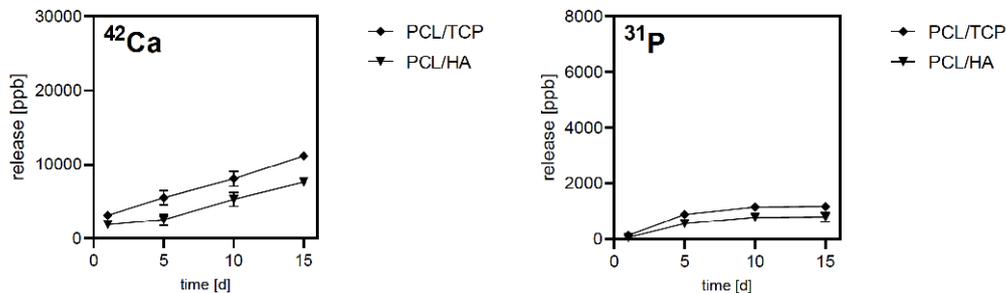

b) Degradation in PBS w. 0.4 mg/ml lipsase
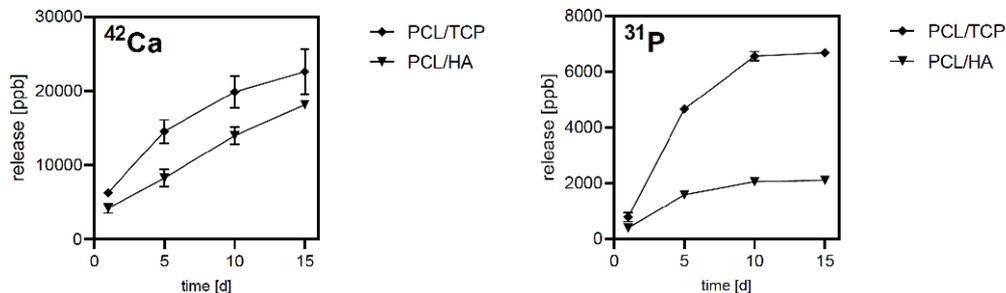
Figure 11: Ion release from PCL/HA and PCL/TCP ceramic discs over 15 days after immersion in a) PBS or b) 0.4 mg/ml lipase respectively

3.4. *In vitro* experiment

The experimental set-up for the *in vitro* experiment consisted of chondrocytes seeded directly onto a ceramic disc or encapsulated in GelMA and then placed on a ceramic disc (Figure 8). There are two reasons for this. Since the solvents (DCM, 2-Bu and DBP) used to dissolve the PCL-bioceramic mixture are all cytotoxic, constructs were washed with water and ethanol prior to the *in vitro* experiment (Jakus et al., 2016). However, to confirm whether the washing process was successful at removing the solvents, we explored seeding a pellet of equine chondrocytes directly onto the ceramic disc. The second reason is to investigate whether cells in direct contact with Ca and P ions (cell seeded disc) from the ceramic disc show a higher matrix deposition compared to cells in the hydrogel. We hypothesize that cells in the hydrogel likely are less influenced by the osteogenic ions, since the ions must diffuse into the gel and come in contact with cells in order to exert their effect.

3.4.1. Cell viability

The cell seeded discs have on average a higher cell viability at all time points compared to the cells in GelMA. The cells in GelMA groups show a gradual increase in cell viability from day 1 to 28, while the cell seeded discs already have a high viability on day 1, which remains high until day 28. At day 28, the cell viability for three of the groups is over 90%, while the cells in GelMA 70% HA has a viability of 75%. On the whole, the samples have a good biocompatibility, due to the relatively high percentage cell viability of around 80%, as seen in Figure 12.

3.4.2. Cell metabolic activity
All the groups indicate an increase in cell metabolic activity over 28 days, evidenced by increase in fluorescence (Figure 13). Interestingly, 3 groups have a statistically significant increase between the cell metabolic activity from day 1 to day 28. The group 'cells in GelMA 70% TCP' is the only group in which the increase in cell metabolic activity is not statistically significant. Overall, the Alamar blue assay indicates an increase in cell number due to cell proliferation.

3.4.3. Amount of GAGs relative to amount of DNA
In the present study, the DMMB/ Picogreen assay indicates that the chondrocytes produce a very low amount of GAGs/ DNA of about 0.5-2 µg/µg in all groups. Figure 14 shows a plot of the GAGs/ DNA. Due to the use of the same cell type, cell culture media and cell seeding density, the results of the present study can be compared with a 2019 study by Castilho et al. (Castilho et al., 2019). The study used a micro-fibre architecture to reinforce a GelMA hydrogel system. Equine chondrocytes were encapsulated in GelMA at a seeding density of $20* 10^6$ cells/ml, and constructs were cultured in a media containing TGF β1. By day 28, the chondrocytes had produced 40-50 µg/µg of GAGs/DNA (depending on the type of microfibre reinforcement for the hydrogel). In the present study, the cells in the present study remain viable and metabolically active, as evidenced from the LIVE/DEAD assay and Alamar blue assay, yet produce a small amount of GAGs.
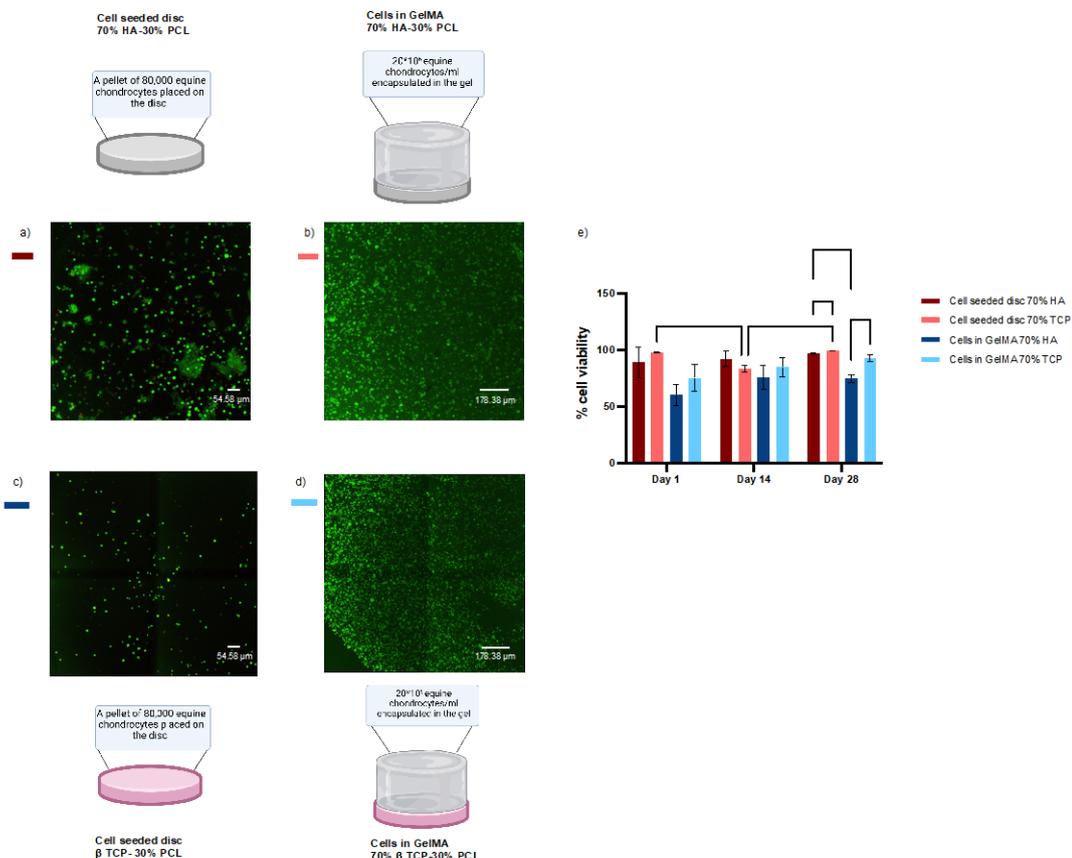

Figure 12: Confocal images of LIVE/ DEAD assay staining at Day 1 for a) cell seeded disc 70% HA, b) cell seeded disc 70% β-TCP, c) cells in GelMA 70% HA, d) cells in GelMA 70% β-TCP. e) Quantified results of the LIVE/ DEAD assay comparing all four groups over 28 days. * p < 0. 05, ** p < 0. 01, *** p < 0.001 and **** p < 0.0001
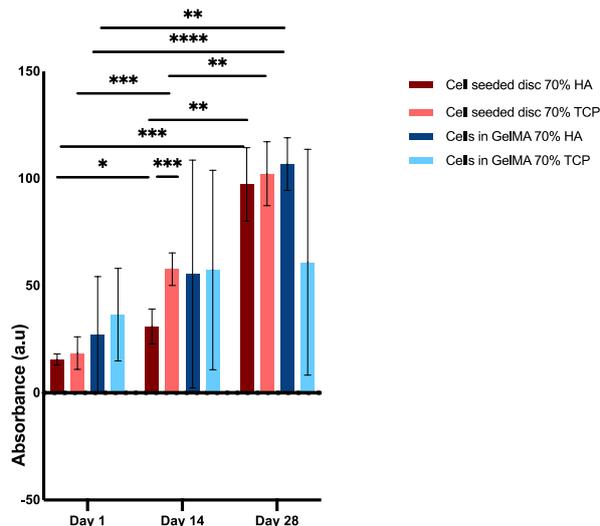
Figure 13: Alamar blue assay indicates cell metabolic activity, higher absorbance indicates higher metabolic activity. * p < 0. 05, ** p < 0. 01, *** p < 0.001 and **** p < 0.0001
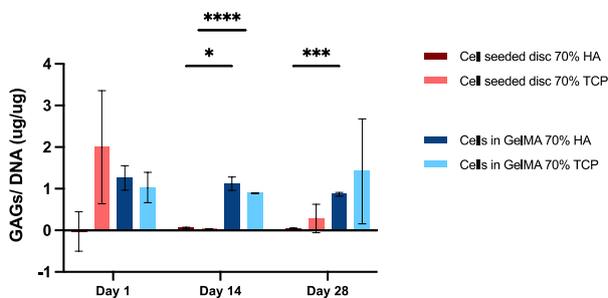

Figure 14: DMMB/ Picogreen assay reveals the amount of GAGs normalized to the amount of DNA in µg/µg. * p < 0. 05, ** p < 0. 01

3.4.4. Safranin-O, Collagen type I and Collagen type II

In the Safranin-O stain, proteoglycans are stained red, while collagens are stained green and cell nuclei are stained dark blue. All of the groups produce only small amounts of GAGs even at day 28, except the group of cells in GelMA 70%HA (Figure 15 a, b, d). The group of 'cells in GelMA 70% HA', produces proteoglycans at both day 14 and day 28 (Figure 15 c), which appear to be in the pericellular area predominantly. The small amount of GAGs seen in this staining is corroborated by the DMMB/ Picogreen assay. Importantly, the deposition of a tidemark layer is not observed in any of the groups. The tidemark layer forms the border between articular cartilage and calcified cartilage, and appears as a dense purple band, when stained by hematoxylin (Hoemann et al., 2012).

Immunohistochemistry was performed on the tissue samples to visualize Collagen type I and Collagen type II. Collagens are stained brown. Collagen type II is not observed in any of the groups at any time point (Figure S1). The presence of Collagen type I, on the other hand, can be seen in all the groups at day 28. In the cell seeded discs, Collagen type I is present around the cells, and cells surrounded by Collagen type I are present at the edges of the tissue sample (Figure 16 a and b). In the cells in GelMA samples on the other hand, a strong collagen type I staining is observed at the edges of the sample, as well as a fainter stain around the cell nuclei, which are uniformly distributed through the sample (Figure 16 c and d). All the groups are characterized by the presence of small amounts of GAGs and no Collagen type II. In addition, Collagen type I is observed in all samples, with the collagens being distributed more evenly in the GelMA samples and present around the edges in the cell seeded discs. The presence of Collagen type I and absence of Collagen type II could be due to the de-differentiation of chondrocytes during monolayer culture into a fibroblastic lineage (Camarero-Espinosa et al., 2016; Holtzer et al., 1960). To verify whether chondrocytes in the present study became hypertrophic and deposit a mineralized matrix, other analyses such as a Collagen type X staining, and an ALP assay should be performed. Collagen type X and alkaline phosphatases (ALP) are characteristic biomarkers for calcified cartilage tissue. Further, performing a picosirius red staining, RT-qPCR, and SEM-EDX would enable a more detailed characterization of the newly deposited matrix.

a) Cell seeded disc
   70% HA-30% PCL

b) Cell seeded disc
   β TCP- 30% PCL

c) Cells in GelMA
   70% HA-30% PCL

d) Cells in GelMA
   70% β TCP-30% PCL

e) Positive control: rat
   knee growth plate
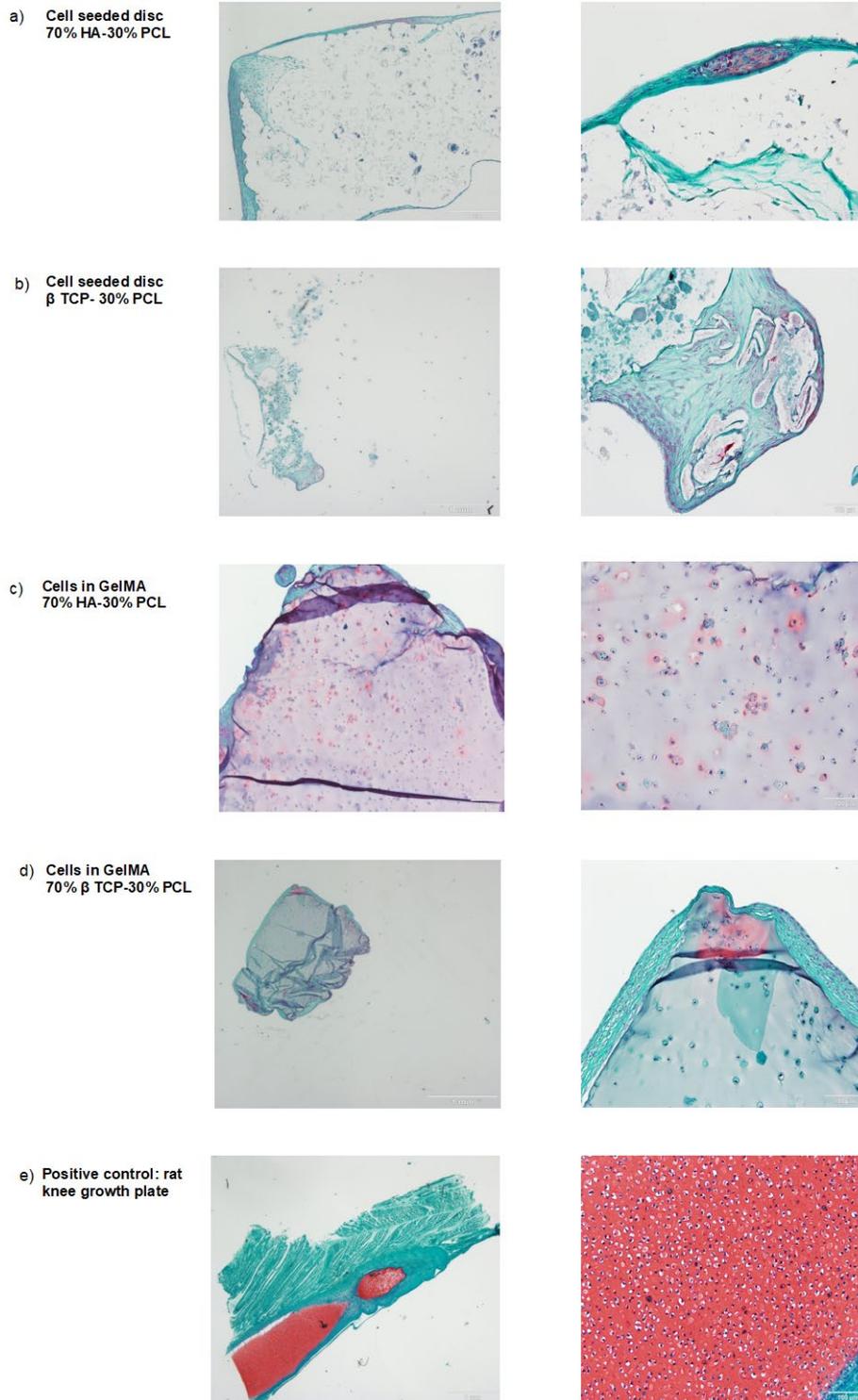
Figure 15: Safranin-O staining of a) cell seeded disc 70% HA, b) cell seeded disc 70% β-TCP, c) cells in GelMA 70% HA, d) cells in GelMA, e) positive control of a rat knee growth plate. Proteoglycans=red, collagens= green and cell nuclei dark =blue.
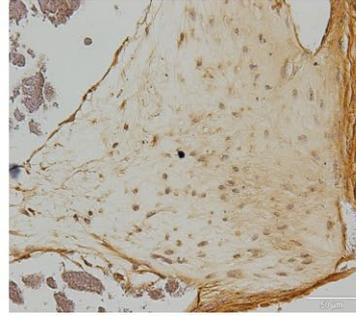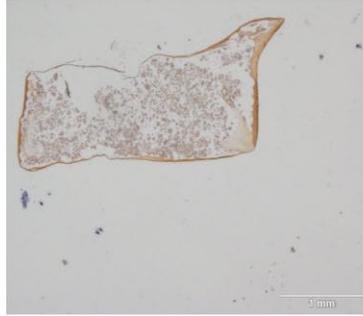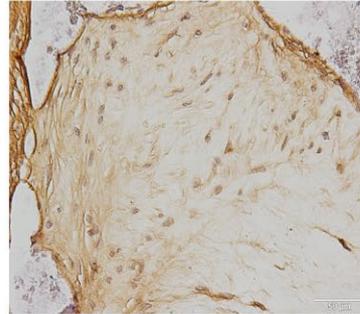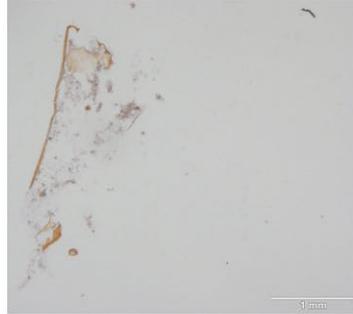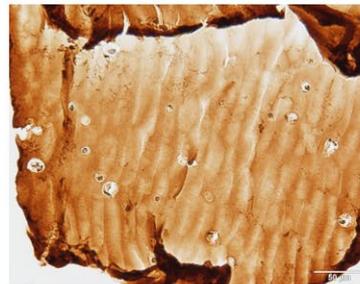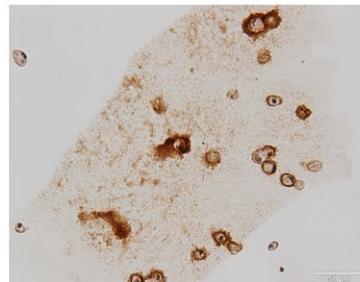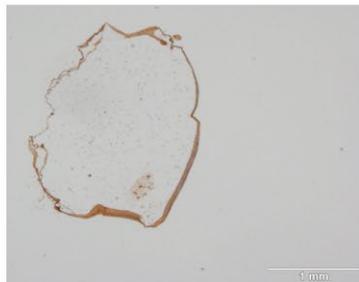
Figure 16: Immunohistochemistry Collagen type I of a) cell seeded disc 70% HA, b) cell seeded disc 70% β-TCP, c) cells in GelMA 70% HA, d) cells in GelMA, e) positive control of human fetal intravertebral disc. Collagen I = brown and cell nuclei dark =blue.

3.5. Conclusion

It is estimated that 654 million people wordlwide suffer from knee osteoarthritis (Cui et al., 2020). Osteoarthritis is a degenerative disease of the joints, which is caused by trauma or aging. Since osteoarthritis is a common cause of disability and impaired quality of life, especially in the elderly, it is the need of the hour to find solutions. While knee osteoarthritis affects the entire joint capsule, surgical interventions have primarily focussed on cartilage repair. The most common surgical treatments for OA include ACI, MACI, microfracture, autografts, allografts and in extreme cases total knee replacement (Camarero-Espinosa et al., 2016; Fortin et al., 2002). Tissue engineering represents a promising alternative for the treatment of OA. Tissue engineering studies which focus on cartilage report compressive and shear moduli which are less than native cartilage (Lepage et al., 2019). The biomechanical inferiority can be addressed by engineering the osteochondral unit as a whole, rather than only focussing on cartilage. Historically, biphasic scaffolds have been widely used for osteochondral tissue engineering, comprising of a hydrogel phase for the chondral tissue and a bioceramic phase for the osteal tissue. These types of scaffolds suffer from phase delamination and poor interagration with native tissue *in vivo* (Diloksumpan et al., 2020, 2021). The critical role of calcified cartilage in providing a secure mechanically competent interface between viscoelastic cartilage and stiff bone cannot be understated (Choe et al., 2021; Doyle et al., 2021; Goldring & Goldring, 2016; Lepage et al., 2019; Madry et al., 2010). Relatively few studies have focussed on engineering calcified cartilage.

In this study we present a novel biomaterial ink composed of β-TCP-PCL for engineering calcified cartilage tissue. First, we found that the same tri-solvent mixture used by Jakus et al. to produce a HA-PCL biomaterial ink, can be used to produce β-TCP-PCL blends. One difference between our study and that of Jakus et al. is that they used microparticles, while we use nanoparticles of HA and β-TCP since native cartilage and bone is nano-structured. The shape fidelity of three ratios (volume-volume%) of HA-PCL and β-TCP-PCL were investigated through the filament collapse test and filament fusion test, allowing for a quantitative analysis of shape fidelity rather than a simple macroscopic or microscopic evaluation. The filament collapse test indicates that the compositions with the highest ceramic content have the highest yield stress, and consequently best shape fidelity. However the yield stress of these materials should also be obtained through rheological measurements to compare the experimental yield stress to that obtained through the theoretical model of Ribeiro et al. (Ribeiro et al., 2018). On the other hand, the filament fusion test indicates that a minimum interfibre spacing of 0.5- 1 mm for all groups, indicating a similar printing resolution. For the rest of the study 70%HA- 30% PCL and 70% β-TCP -30% PCL were used due to their best shape fidelity and similar resolution in the x-y plane compared to other concentrations.

Next, we assessed whether the two polymer-ceramic blends can be used to fabricate porous bone scaffolds via solvent-based extrusion printing. Both materials produce porous scaffolds, with a slightly larger filament diameter and pore size seen in the 70% HA-30% PCL scaffold, even with the same CAD file. The pore sizes of both scaffolds are in the range conducive to bone growth (300-900 µm). Tensile tests should be performed on these scaffolds to assess whether the pores compromise the mechanical properties and whether they are comparable to that of native bone. In addition, micro-CT should be performed to analyse porosity and pore interconnectivity, which are critical to cell ingrowth and proliferation and vascularization *in vivo* (Mohammadi et al., 2021; Xiao et al., 2020).

We performed a degradation assay comparing the release of Ca and P ions from the ceramic discs composed of 70% HA-30% PCL and 70% β-TCP -30% PCL. As hypothesized, due to the higher solubility of β-TCP, the β-TCP-PCL blend releases more Ca and P ions over 21 days, compared to the HA group. The differences in ion release are more prominent under enzymatic conditions. Importantly, the thermoplast is not masking the ceramic component, indicating the advantage of solvent-based extrusion printing over hot-melt FDM.

Next an *in vitro* study was performed to asssess if the release of osteogenic ions induces the production of calcified cartilage tissue. Consistent with their anatomical presence, chondrocytes of equine origin were used. The hypothesis is that the β-TCP-PCL would induce chondrocyte hypertrophy faster and the faster production of mineralized matrix than HA- PCL due to the higher release of osteogenic ions. In all four experimental groups chondrocytes remained viable and metabolically active over 28 days. Since cells seeded directly onto ceramic discs were viable and metabolically active, this indicates the success of the washing procedure to remove the cytotoxic solvents. The chondrocytes in all groups

produce a small amount of GAGs (normalized to DNA) of about 0-2 µg/µg. Immunohistochemistry stainings reveal that Collagen type II is not produced by any of the groups. Collagen type I on the other and is produced by all groups at day 28 and shows a more uniform distrubution in the tissue samples of cells encapsulated in GelMA. The presence of Collagen type I and absence of GAGs and Collagen type II likely indicates de-differentiated chondrocytes producing fibrocartilage. Fibrocartilage, characterized by Collagen type I has insufficient mechanical properties to support joint loading. Since the IHC results are qualitative, they should be considered carefully. The amount of Collagen type X and ALPs, which are key biomarkers for calcified cartilage, should be investigated to ascertain if chondrocytes are induced into a hypertrophic lineage by the presence of osteogenic ions. This is because native calcified cartilage ECM is composed of Collagen type II, Collagen type X and GAGs as well as alkaline phosphatase. Therefore, more evidence is needed to truly say whether the higher soluble β-TCP is more effective at producing a calcified cartilage matrix.

In conclusion, we present a novel bioink composed of β-TCP-PCL for calcified cartilage tissue engineering. This bioink can be processed with solvent-based extrusion printing in the same way as the established bioink composed of HA-PCL. Both β-TCP-PCL and HA-PCL can be used to fabricate porous scaffolds, with pore sizes in the range that is conducive to bone ingrowth. With the solvent-based extrusion, the thermoplast component is not masking the release of calcium and phosphorous ions, indicating the advantage of this technique over hot melt FDM. Chondrocytes encapsulated in GelMA or seeded directly onto ceramic discs of β-TCP-PCL and HA-PCL remain viable and metabolically active, and likely produce fibrocartilaginous matrix. Due to the critical role of the calcified cartilage in providing a mechanically competent interface between articular cartilage and bone, future research should focus on optimizing a bioink for calcified cartilage tissue engineering.

3.6. Suggestions for future studies

Adult calcified cartilage tissue is composed of Collagen type II, Collagen type X and GAGs as well as alkaline phosphatases. Collagen type X can be visualized through immunohistochemistry. In addition to the types of collagens produced, the orientation of collagen fibrils contributes to the biomechanical function of the calcified zone. Collagen fibrils in the calcified cartilage layer are arranged perpendicular to the articulating surface. A previous study reported using polarized light on samples stained with Picosirius red (which stains Collagen type I) to investigate collagen orientation (Golafshan et al., 2020). The ALP assay is ubiquitously used as an early marker of osteoblast differentiation, usually showing an increase in the first week followed by decline later (Gerdes et al., 2020). Alkaline phosphatase is an enzyme which is highly expressed in the plasma membrane of hypertrophic chondrocytes and osteoblasts. They catalyze the hydrolysis of pyrophosphates, which is an inhibitor of bone mineralization, and convert organic phosphates into inorganic phosphates. Inorganic phosphate ions are responsible for hydroxyapatite nucleation and creation. ALP assays measure enzyme activity by using p-nitrophenyl phosphate (pNPP) as an enzyme substrate that turns yellow (λmax= 405 nm) when dephosphorylated by ALP (Sekaran et al., 2021).

While immunohistochemistry and histology provide a qualitative understanding of the composition of the newly deposited tissue, gene expression of various chondrogenic and osteogenic genes should be investigated. Chondrogenic genes include, COL2 (Collagen type II) and ACAN (aggrecan) and osteogenic genes include COL1 (Collagen type I), COL10 (Collagen type X), ALPL (alkaline phosphatase), BGLAP (osteocalcin), BSP (bone sialoprotein), Runx-2 (Runt-related transcription factor 2) and MMP-13 (matrix metalloprotein-13). Osteocalcin is a protein synthesized by hypertrophic chondrocytes that undergo osteogenic transdifferentiation. Bone sialoprotein is a phosphoprotein found in bone tissue and is considered a late marker of bone mineralization. Runx-2 is a transcription factor that influences the early differentiation of MSCs into osteogenic pathways by upregulating ALP, osteocalcin, osteopontin and BSP. In calcified cartilage tissue, we would expect COL2, ACAN, ALPL, COL10, Runx-2 and MMP-13 to be upregulated. Since BGLAP and BSP are later markers of mineralization they are unlikely to be highly expressed during a 28 day experiment (Kosik-Kozioł et al., 2019; Polini et al., 2011). To obtain a further understanding of the composition of the newly formed tissue, SEM- EDX can enable an analysis of the elements found in the sample, as well as the distribution of calcium and phosphorous ions in the neo-tissue and finally the ratio of Ca:P (Golafshan et al., 2020). Lastly, since the solvents used in extrusion printing are cytotoxic, ceramic discs were washed with water and ethanol prior to the *in vitro* experiment. The cells seeded directly onto the ceramic discs also showed sufficient cell viability and metabolic activity. However, thermogravimetric analysis (TGA) of the ceramic discs would confirm whether the solvents are fully removed by this washing process. The disadvantage is that this washing process is not a clinically approved sterilization procedure. To enable

clinical translation of these constructs, alternative sterilization methods which are FDA approved such as irradiation with gamma rays should employed (Jakus et al., 2016).

Cells seeded on the discs are in direct contact with calcium and phosphorus ions, however a smaller number of cells can be seeded onto the disc (80000 cells). On the other hand, cells in GelMA are not in direct contact with calcium and phosphorous ions, and ions must diffuse into the gel to exert their effect. However, a larger number of cells can be encapsulated in the gel ($2*10^6$) than can be seeded directly on a disc (80000). First, future studies should perform a quantitative comparison of matrix deposition (Collagen type II, Collagen type X, Collagen type I, and ALP) by the two groups. A study of ion diffusion through GelMA can indicate what percentage of ions released from the ceramic discs reach the cells encapsulated in the hydrogel. This will allow us to ascertain which experimental set up should be used in engineering the calcified cartilage zone as well as in the evaluation of a triphasic scaffold.

After optimizing the material for engineering calcified cartilage, future studies should investigate a triphasic osteochondral scaffold, consisting of a chondral, calcified layer and osteal component. We envision the osteal compartment consisting of a microfibre reinforced hydrogel, the calcified zone consisting of layers of the ceramic paste, which functions as a self-adhesive when connected to the osteal component, which is a porous bone scaffold (fabricated as described in section 2.4) (Castilho et al., 2019; Wei & Dai, 2021). In a triphasic construct, properties such an interfacial shear strength should be investigated as well as other mechanical properties that would allow for the constructs to be load bearing in one direction and also be compliant in other directions so that the scaffold can be surgically fitted into an osteochondral defect (Jakus et al., 2016).

Acknowledgements

Reference list

Abbadessa, A., Mouser, V. H. M., Blokzijl, M. M., Gawlitta, D., Dhert, W. J. A., Hennink, W. E., Malda, J., & Vermonden, T. (2016). A Synthetic Thermosensitive Hydrogel for Cartilage Bioprinting and Its Biofunctionalization with Polysaccharides. *Biomacromolecules*, *17*(6), 2137–2147. https://doi.org/10.1021/acs.biomac.6b00366

Barbosa, I., Garcia, S., Barbier-Chassefière, V., Caruelle, J. P., Martelly, I., & Papy-García, D. (2003). Improved and simple micro assay for sulfated glycosaminoglycans quantification in biological extracts and its use in skin and muscle tissue studies. *Glycobiology*, *13*(9), 647–653. https://doi.org/10.1093/glycob/cwg082

Bittner, S. M., Smith, B. T., Diaz-Gomez, L., Hudgins, C. D., Melchiorri, A. J., Scott, D. W., Fisher, J. P., & Mikos, A. G. (2019). Fabrication and mechanical characterization of 3D printed vertical uniform and gradient scaffolds for bone and osteochondral tissue engineering. *Acta Biomaterialia*, *90*, 37–48. https://doi.org/10.1016/j.actbio.2019.03.041

Camarero-Espinosa, S., Rothen-Rutishauser, B., Foster, E. J., & Weder, C. (2016). Articular cartilage: From formation to tissue engineering. *Biomaterials Science*, *4*(5), 734–767. https://doi.org/10.1039/c6bm00068a

Castilho, M., Mouser, V., Chen, M., Malda, J., & Ito, K. (2019). Bi-layered micro-fibre reinforced hydrogels for articular cartilage regeneration. *Acta Biomaterialia*, *95*(xxxx), 297–306. https://doi.org/10.1016/j.actbio.2019.06.030

Choe, R., Devoy, E., Jabari, E., Packer, J. D., & Fisher, J. P. (2021). Biomechanical Aspects of Osteochondral Regeneration: Implications and Strategies for Three-Dimensional Bioprinting. *Tissue Engineering Part B: Reviews*, *00*(00). https://doi.org/10.1089/ten.teb.2021.0101

Cooke, M. E., & Rosenzweig, D. H. (2021). The rheology of direct and suspended extrusion bioprinting. *APL Bioengineering*, *5*(1). https://doi.org/10.1063/5.0031475

Cui, A., Li, H., Wang, D., Zhong, J., Chen, Y., & Lu, H. (2020). Global, regional prevalence, incidence and risk factors of knee osteoarthritis in population-based studies. *EClinicalMedicine*, *29–30*, 100587. https://doi.org/10.1016/j.eclinm.2020.100587

Daghrery, A., de Souza Araújo, I. J., Castilho, M., Malda, J., & Bottino, M. C. (2022). Unveiling the potential of melt electrowriting in regenerative dental medicine. *Acta Biomaterialia*, *xxxx*.

https://doi.org/10.1016/j.actbio.2022.01.010

Diloksumpan, P., Abinzano, F., de Ruijter, M., Mensinga, A., Plomp, S., Khan, I., Brommer, H., Smit, I., Dias Castilho, M., van Weeren, P. R., Malda, J., & Levato, R. (2021). The Complexity of Joint Regeneration: How an Advanced Implant could Fail by Its In Vivo Proven Bone Component. *Journal of Trial and Error*. https://doi.org/10.36850/e3

Diloksumpan, P., De Ruijter, M. ne, Castilho, M., Gbureck, U., Vermonden, T., Van Weeren, P. R., Malda, J., & Levato, R. (2020). Combining multi-scale 3D printing technologies to engineer reinforced hydrogel-ceramic interfaces. *Biofabrication*, *12*(2), 25014. https://doi.org/10.1088/1758-5090/ab69d9

Doyle, S. E., Snow, F., Duchi, S., O'connell, C. D., Onofrillo, C., Di Bella, C., & Pirogova, E. (2021). 3D printed multiphasic scaffolds for osteochondral repair: Challenges and opportunities. *International Journal of Molecular Sciences*, *22*(22). https://doi.org/10.3390/ijms222212420

Farr, J., & Gomoll, A. H. (2018). *Cartilage Restoration: Practical Clinical Applications* (F. Jack & A. H. Gomoll (Eds.); Second Edi). Springer International. https://doi.org/https://doi.org/10.1007/978-3-319-77152-6

Fortin, P. R., Penrod, J. R., Clarke, A. E., St-Pierre, Y., Joseph, L., Bélisle, P., Liang, M. H., Ferland, D., Phillips, C. B., Mahomed, N., Tanzer, M., Sledge, C., Fossel, A. H., & Katz, J. N. (2002). Timing of total joint replacement affects clinical outcomes among patients with osteoarthritis of the hip or knee. *Arthritis and Rheumatism*, *46*(12), 3327–3330. https://doi.org/10.1002/art.10631

Gerdes, S., Mostafavi, A., Ramesh, S., Memic, A., Rivero, I. V., Rao, P., & Tamayol, A. (2020). Process-Structure-Quality Relationships of Three-Dimensional Printed Poly(Caprolactone)-Hydroxyapatite Scaffolds. *Tissue Engineering - Part A*, *26*(5–6), 279–291. https://doi.org/10.1089/ten.tea.2019.0237

Ginebra, M. P., Espanol, M., Maazouz, Y., Bergez, V., & Pastorino, D. (2018). Bioceramics and bone healing. *EFORT Open Reviews*, *3*(5), 173–183. https://doi.org/10.1302/2058-5241.3.170056

Golafshan, N., Vorndran, E., Zaharievski, S., Brommer, H., Kadumudi, F. B., Dolatshahi-Pirouz, A., Gbureck, U., van Weeren, R., Castilho, M., & Malda, J. (2020). Tough magnesium phosphate-based 3D-printed implants induce bone regeneration in an equine defect model. *Biomaterials*, *261*(July). https://doi.org/10.1016/j.biomaterials.2020.120302

Goldring, S. R., & Goldring, M. B. (2016). Changes in the osteochondral unit during osteoarthritis: Structure, function and cartilage bone crosstalk. *Nature Reviews Rheumatology*, *12*(11), 632–644. https://doi.org/10.1038/nrrheum.2016.148

Heughebaert, M., LeGeros, R. Z., Gineste, M., Guilhem, A., & Bonel, G. (1988). Physicochemical characterization of deposits associated with HA ceramics implanted in nonosseous sites. *Journal of Biomedical Materials Research*, *22*(S14), 257–268. https://doi.org/10.1002/jbm.820221406

Hoemann, C. D., Lafantaisie-Favreau, C. H., Lascau-Coman, V., Chen, G., & Guzmán-Morales, J. (2012). The cartilage-bone interface. *The Journal of Knee Surgery*, *25*(2), 85–97. https://doi.org/10.1055/s-0032-1319782

Holtzer, H., Abbott, J., Lash, J., & Holtzer, S. (1960). the Loss of Phenotypic Traits By Differentiated Cells in Vitro, I. Dedifferentiation of Cartilage Cells. *Proceedings of the National Academy of Sciences*, *46*(12), 1533–1542. https://doi.org/10.1073/pnas.46.12.1533

Huang, B., Caetano, G., Vyas, C., Blaker, J. J., Diver, C., & Bártolo, P. (2018). Polymer-ceramic composite scaffolds: The effect of hydroxyapatite and β-tri-calcium phosphate. *Materials*, *11*(1). https://doi.org/10.3390/ma11010129

Hunter, D. J., & Bierma-Zeinstra, S. (2019). Osteoarthritis. *The Lancet*, *393*(10182), 1745–1759. https://doi.org/10.1016/S0140-6736(19)30417-9

Jakus, A. E., Rutz, A. L., Jordan, S. W., Kannan, A., Mitchell, S. M., Yun, C., Koube, K. D., Yoo, S. C., Whiteley, H. E., Richter, C. P., Galiano, R. D., Hsu, W. K., Stock, S. R., Hsu, E. L., & Shah, R. N. (2016). Hyperelastic "bone": A highly versatile, growth factor-free, osteoregenerative, scalable, and surgically friendly biomaterial. *Science Translational Medicine*, *8*(358), 1–16. https://doi.org/10.1126/scitranslmed.aaf7704

Kim, J. W., Shin, K. H., Koh, Y. H., Hah, M. J., Moon, J., & Kim, H. E. (2017). Production of poly(ε-caprolactone)/hydroxyapatite composite scaffolds with a tailored macro/micro-porous structure, high mechanical properties, and excellent bioactivity. *Materials*, *10*(10). https://doi.org/10.3390/ma10101123

Kimber, K., & Shelton, W. (2010). Cartilage restoration. In *Minerva Ortopedica e Traumatologica* (Vol. 61, Issue 4). https://doi.org/10.1007/978-3-319-77152-6

Konopnicki, S., Sharaf, B., Resnick, C., Patenaude, A., Pogal-Sussman, T., Hwang, K. G., Abukawa, H., & Troulis, M. J. (2015). Tissue-engineered bone with 3-dimensionally printed β-tricalcium

phosphate and polycaprolactone scaffolds and early implantation: An in vivo pilot study in a porcine mandible model. *Journal of Oral and Maxillofacial Surgery*, *73*(5), 1016.e1-1016.e11. https://doi.org/10.1016/j.joms.2015.01.021

Kosik-Kozioł, A., Costantini, M., Mróz, A., Idaszek, J., Heljak, M., Jaroszewicz, J., Kijeńska, E., Szöke, K., Frerker, N., Barbetta, A., Brinchmann, J. E., & Święszkowski, W. (2019). 3D bioprinted hydrogel model incorporating β-tricalcium phosphate for calcified cartilage tissue engineering. *Biofabrication*, *11*(3). https://doi.org/10.1088/1758-5090/ab15cb

Kumar, P., Nagarajan, A., & Uchil, P. D. (2018). Analysis of cell viability by the alamarblue assay. *Cold Spring Harbor Protocols*, *2018*(6), 462–464. https://doi.org/10.1101/pdb.prot095489

Kwon, H., Brown, W. E., Lee, C. A., Wang, D., Paschos, N., Hu, J. C., & Athanasiou, K. A. (2019). Surgical and tissue engineering strategies for articular cartilage and meniscus repair. *Nature Reviews Rheumatology*, *15*(9), 550–570. https://doi.org/10.1038/s41584-019-0255-1

Lepage, S. I. M., Robson, N., Gilmore, H., Davis, O., Hooper, A., St John, S., Kamesan, V., Gelis, P., Carvajal, D., Hurtig, M., & Koch, T. G. (2019). Beyond Cartilage Repair: The Role of the Osteochondral Unit in Joint Health and Disease. *Tissue Engineering - Part B: Reviews*, *25*(2), 114–125. https://doi.org/10.1089/ten.teb.2018.0122

Lin, H., Lozito, T. P., Alexander, P. G., Gottardi, R., & Tuan, R. S. (2014). Stem cell-based microphysiological osteochondral system to model tissue response to interleukin-1B. *Molecular Pharmaceutics*, *11*(7), 2203–2212. https://doi.org/10.1021/mp500136b

Liu, J., Li, L., Suo, H., Yan, M., Yin, J., & Fu, J. (2019). 3D printing of biomimetic multi-layered GelMA/nHA scaffold for osteochondral defect repair. *Materials and Design*, *171*, 107708. https://doi.org/10.1016/j.matdes.2019.107708

LIVE/DEAD™ Viability/Cytotoxicity Kit, for mammalian cells. (n.d.). Thermo Fischer SCIENTIFIC.

Madry, H., van Dijk, C. N., & Mueller-Gerbl, M. (2010). The basic science of the subchondral bone. *Knee Surgery, Sports Traumatology, Arthroscopy*, *18*(4), 419–433. https://doi.org/10.1007/s00167-010-1054-z

Mancini, I. A. D., Schmidt, S., Brommer, H., Pouran, B., Schäfer, S., Tessmar, J., Mensinga, A., Van Rijen, M. H. P., Groll, J., Blunk, T., Levato, R., Malda, J., & Van Weeren, P. R. (2020). A composite hydrogel-3D printed thermoplast osteochondral anchor as example for a zonal approach to cartilage repair: In vivo performance in a long-term equine model. *Biofabrication*, *12*(3). https://doi.org/10.1088/1758-5090/ab94ce

Mohammadi, H., Sepantafar, M., Muhamad, N., & Bakar Sulong, A. (2021). How Does Scaffold Porosity Conduct Bone Tissue Regeneration? *Advanced Engineering Materials*, *23*(10), 1–19. https://doi.org/10.1002/adem.202100463

Moroni, L., Boland, T., Burdick, J. A., De Maria, C., Derby, B., Forgacs, G., Groll, J., Li, Q., Malda, J., Mironov, V. A., Mota, C., Nakamura, M., Shu, W., Takeuchi, S., Woodfield, T. B. F., Xu, T., Yoo, J. J., & Vozzi, G. (2018). Biofabrication: A Guide to Technology and Terminology. *Trends in Biotechnology*, *36*(4), 384–402. https://doi.org/10.1016/j.tibtech.2017.10.015

Mouser, V. H. M., Abbadessa, A., Levato, R., Hennink, W. E., Vermonden, T., Gawlitta, D., & Malda, J. (2017). Development of a thermosensitive HAMA-containing bio-ink for the fabrication of composite cartilage repair constructs. *Biofabrication*, *9*(1), 15026. https://doi.org/10.1088/1758-5090/aa6265

Musumeci, G. (2016). The effect of mechanical loading on articular cartilage. *Journal of Functional Morphology and Kinesiology*, *1*(2), 154–161. https://doi.org/10.3390/jfmk1020154

Nyberg, E., Rindone, A., Dorafshar, A., & Grayson, W. L. (2017). Comparison of 3D-Printed Poly-ϵ-Caprolactone Scaffolds Functionalized with Tricalcium Phosphate, Hydroxyapatite, Bio-Oss, or Decellularized Bone Matrix. *Tissue Engineering - Part A*, *23*(11–12), 503–514. https://doi.org/10.1089/ten.tea.2016.0418

Ogose, A., Hotta, T., Kawashima, H., Kondo, N., Gu, W., Kamura, T., & Endo, N. (2005). Comparison of hydroxyapatite and beta tricalcium phosphate as bone substitutes after excision of bone tumors. *Journal of Biomedical Materials Research - Part B Applied Biomaterials*, *72*(1), 94–101. https://doi.org/10.1002/jbm.b.30136

Park, -->JiSun, Jin, S., Hyeon, H., Hee, J., Doo, W., Young, J., & Park, S. A. (2016). Phosphate / Polycaprolactone Scaffolds for Dental Tissue Engineering. *Journal of Industrial and Engineering Chemistry*, *46*, 175–181. http://linkinghub.elsevier.com/retrieve/pii/S1226086X16304075%0Ahttp://dx.doi.org/10.1016/j.jiec.2016.10.028

Piluso, S., Li, Y., Abinzano, F., Levato, R., Moreira Teixeira, L., Karperien, M., Leijten, J., van Weeren, R., & Malda, J. (2019). Mimicking the Articular Joint with In Vitro Models. *Trends in Biotechnology*, *37*(10), 1063–1077. https://doi.org/10.1016/j.tibtech.2019.03.003

Polini, A., Pisignano, D., Parodi, M., Quarto, R., & Scaglione, S. (2011). Osteoinduction of human mesenchymal stem cells by bioactive composite scaffolds without supplemental osteogenic growth factors. *PLoS ONE*, *6*(10), 1–8. https://doi.org/10.1371/journal.pone.0026211

Pouran, B., Arbabi, V., Bleys, R. L., René van Weeren, P., Zadpoor, A. A., & Weinans, H. (2017). Solute transport at the interface of cartilage and subchondral bone plate: Effect of micro-architecture. *Journal of Biomechanics*, *52*, 148–154. https://doi.org/10.1016/j.jbiomech.2016.12.025

Ribeiro, A., Blokzijl, M. M., Levato, R., Visser, C. W., Castilho, M., Hennink, W. E., Vermonden, T., & Malda, J. (2018). Assessing bioink shape fidelity to aid material development in 3D bioprinting. *Biofabrication*, *10*(1), 14102. https://doi.org/10.1088/1758-5090/aa90e2

Schwab, A., Levato, R., D'Este, M., Piluso, S., Eglin, D., & Malda, J. (2020). Printability and Shape Fidelity of Bioinks in 3D Bioprinting. *Chemical Reviews*, *120*(19), 11028–11055. https://doi.org/10.1021/acs.chemrev.0c00084

Sekaran, S., Selvaraj, V., & Thangavelu, L. (2021). The physiological and pathological role of tissue nonspecific alkaline phosphatase beyond mineralization. *Biomolecules*, *11*(11), 1–21. https://doi.org/10.3390/biom11111564

Sheikh, Z., Abdallah, M. N., Hanafi, A. A., Misbahuddin, S., Rashid, H., & Glogauer, M. (2015). Mechanisms of in vivo degradation and resorption of calcium phosphate based biomaterials. *Materials*, *8*(11), 7913–7925. https://doi.org/10.3390/ma8115430

St-Pierre, J. P., Gan, L., Wang, J., Pilliar, R. M., Grynpas, M. D., & Kandel, R. A. (2012). The incorporation of a zone of calcified cartilage improves the interfacial shear strength between in vitro-formed cartilage and the underlying substrate. *Acta Biomaterialia*, *8*(4), 1603–1615. https://doi.org/10.1016/j.actbio.2011.12.022

Tang, Z., Li, X., Tan, Y., Fan, H., & Zhang, X. (2018). The material and biological characteristics of osteoinductive calcium phosphate ceramics. *Regenerative Biomaterials*, *5*(1), 43–59. https://doi.org/10.1093/rb/rbx024

Wang, Q., Ye, W., Ma, Z., Xie, W., Zhong, L., Wang, Y., & Rong, Q. (2021). 3D printed PCL/β-TCP cross-scale scaffold with high-precision fiber for providing cell growth and forming bones in the pores. *Materials Science and Engineering C*, *127*(May). https://doi.org/10.1016/j.msec.2021.112197

Wei, W., & Dai, H. (2021). Articular cartilage and osteochondral tissue engineering techniques: Recent advances and challenges. *Bioactive Materials*, *6*(12), 4830–4855. https://doi.org/10.1016/j.bioactmat.2021.05.011

Xiao, D., Zhang, J., Zhang, C., Barbieri, D., Yuan, H., Moroni, L., & Feng, G. (2020). The role of calcium phosphate surface structure in osteogenesis and the mechanisms involved. *Acta Biomaterialia*, *106*, 22–33. https://doi.org/10.1016/j.actbio.2019.12.034

Yang, J., Zhang, Y. S., Yue, K., & Khademhosseini, A. (2017). Cell-laden hydrogels for osteochondral and cartilage tissue engineering. *Acta Biomaterialia*, *57*, 1–25. https://doi.org/10.1016/j.actbio.2017.01.036

Yue, K., Santiago, G. T., Tamayol, A., Annabi, N., Khademhosseini, A., Hospital, W., Arabia, S., Trujillo-de Santiago, G., Alvarez, M. M., Tamayol, A., Annabi, N., & Khademhosseini, A. (2016). Synthesis, properties, and biomedical applications of gelatin methacryloyl (GelMA) hydrogels. *Biomaterials*, *73*(3), 254–271. https://doi.org/10.1016/j.biomaterials.2015.08.045.Synthesis

Zhang, B., Huang, J., & Narayan, R. J. (2020). Gradient scaffolds for osteochondral tissue engineering and regeneration. *Journal of Materials Chemistry B*, *8*(36), 8149–8170. https://doi.org/10.1039/d0tb00688b

Zhang, Y. S., Haghiashtiani, G., Hübscher, T., Kelly, D. J., Lee, J. M., Lutolf, M., McAlpine, M. C., Yeong, W. Y., Zenobi-Wong, M., & Malda, J. (2021). 3D extrusion bioprinting. *Nature Reviews Methods Primers*, *1*(1). https://doi.org/10.1038/s43586-021-00073-8

Zhou, L., Gjvm, V. O., Malda, J., Stoddart, M. J., Lai, Y., Richards, R. G., Ki-wai Ho, K., & Qin, L. (2020). Innovative Tissue-Engineered Strategies for Osteochondral Defect Repair and Regeneration: Current Progress and Challenges. *Advanced Healthcare Materials*, *9*(23), 1–22. https://doi.org/10.1002/adhm.202001008

Supplementary Information

a) Cell seeded disc
   70% HA-30% PCL

b) Cell seeded disc
   β TCP- 30% PCL

c) Cells in GelMA
   70% HA-30% PCL

d) Cells in GelMA
   70% β TCP-30% PCL

e) Positive control
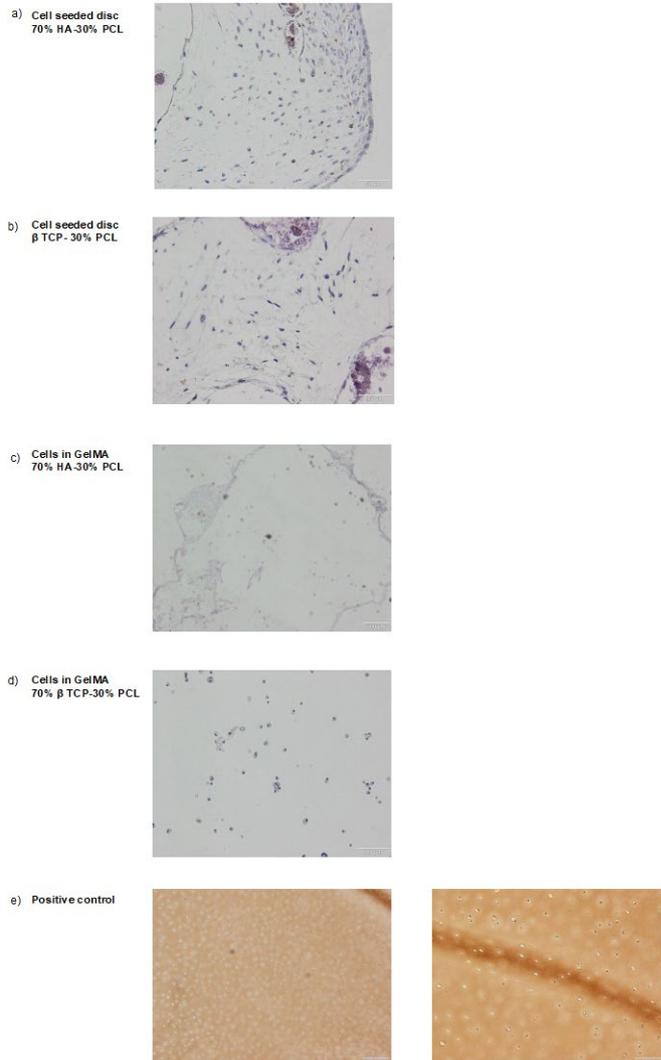
Figure S1: IHC Collagen type II stain at day 28

S2: G-code for the filament collapse test

```
%
(RegenHU)
(Generated with BioCad V1.1)
(File: filament collapse test)
(http://www.regenhu.com/)
(Date : 19.12.2018)

(Program-Start)
G90 G94
```

```
(PARALLEL PRINTING)
(Beginning [Object 01-Group 01-Level 01-Layer 01])
G76 Z0
M99
M90 P2 D2
M95 P1
G0 X0 Y-5
G0 Z0
M97
F15 G1 X0 Y50
M96
G0 Z0.1
M98
(Ending [Object 01-Group 01-Level 01-Layer 01])

(Program-End)
G76 Z0
G0 X0 Y0
M2
```

S3: G-code for the filament fusion test
```
(Program-Start)
G90 G94

(PARALLEL PRINTING)
(Beginning [Object 01-Group 01-Level 01-Layer 02])
G76 Z0
M99
M90 P2 D1; (Choose printhead)
M95 P2

G0 X-20 Y-5; (starting position)
G0 Z0

M97; (start dispensing)

G91
G1 F10  X0 Y0 ; (F=speed)

G24 N5 ;Loop
G1 Y10
G1 X0.25
G1 Y-10
G1 X0.25
G98

G24 N5 ;Loop
G1 Y10
G1 X0.5
G1 Y-10
G1 X0.5
G98

G24 N2 ;Loop
G1 Y10
G1 X1
G1 Y-10
G1 X1
G98
```

```
G24 N5 ;Loop
G1 Y10
G1 X1.5
G1 Y-10
G1 X1.5
G98

G24 N5 ;Loop
G1 Y10
G1 X2
G1 Y-10
G1 X2
G98

G24 N5 ;Loop
G1 Y10
G1 X2.5
G1 Y-10
G1 X2.5
G98

G24 N5 ;Loop
G1 Y10
G1 X3
G1 Y-10
G1 X3
G98

G24 N5 ;Loop
G1 Y10
G1 X3.5
G1 Y-10
G1 X3.5
G98

G24 N5 ;Loop
G1 Y10
G1 X4
G1 Y-10
G1 X4
G98

G24 N5 ;Loop
G1 Y10
G1 X4.5
G1 Y-10
G1 X4.5
G98

G24 N5 ;Loop
G1 Y10
G1 X5
G1 Y-10
G1 X5
G98


M96
```

```
G0 Z30.000
G0 X0.000  Y0.000
M2
```

S4: G-code for the fabrication of a bone scaffold

```
%
(RegenHU)
(Generated with BioCad V1.1)
(File: rectangular for3scaf)
(http://www.regenhu.com/)
(Date : 29.09.2020)

(Program-Start)
G90 G94

(PARALLEL PRINTING)
(Beginning [Object 01-Group 01-Level 01-Layer 02])
G76 Z0
M99
M90 P2 D2
M95 P1
G0 X-23 Y5.5
G0 Z0
M97
F6 G1 X23 Y5.5
X23 Y4.5
X-23 Y4.5
X-23 Y3.5
X23 Y3.5
X23 Y2.5
X-23 Y2.5
X-23 Y1.5
X23 Y1.5
X23 Y0.5
X-23 Y0.5
X-23 Y-0.5
X23 Y-0.5
X23 Y-1.5
X-23 Y-1.5
X-23 Y-2.5
X23 Y-2.5
X23 Y-3.5
X-23 Y-3.5
X-23 Y-4.5
X23 Y-4.5
X23 Y-5.5
X-23 Y-5.5
X-23 Y-6.5
X23 Y-6.5
M96
G0 Z0.1
(Ending [Object 01-Group 01-Level 01-Layer 02])

(Beginning [Object 01-Group 01-Level 02-Layer 03])
G0 Z0.3
G0 X22 Y6.5
G0 Z0.2
M97
G1 X22 Y-6.5
```

```
X21 Y-6.5
X21 Y6.5
X20 Y6.5
X20 Y-6.5
X19 Y-6.5
X19 Y6.5
X18 Y6.5
X18 Y-6.5
X17 Y-6.5
X17 Y6.5
X16 Y6.5
X16 Y-6.5
X15 Y-6.5
X15 Y6.5
X14 Y6.5
X14 Y-6.5
X13 Y-6.5
X13 Y6.5
X12 Y6.5
X12 Y-6.5
X11 Y-6.5
X11 Y6.5
X10 Y6.5
X10 Y-6.5
X9 Y-6.5
X9 Y6.5
X8 Y6.5
X8 Y-6.5
X7 Y-6.5
X7 Y6.5
X6 Y6.5
X6 Y-6.5
X5 Y-6.5
X5 Y6.5
X4 Y6.5
X4 Y-6.5
X3 Y-6.5
X3 Y6.5
X2 Y6.5
X2 Y-6.5
X1 Y-6.5
X1 Y6.5
X0 Y6.5
X0 Y-6.5
X-1 Y-6.5
X-1 Y6.5
X-2 Y6.5
X-2 Y-6.5
X-3 Y-6.5
X-3 Y6.5
X-4 Y6.5
X-4 Y-6.5
X-5 Y-6.5
X-5 Y6.5
X-6 Y6.5
X-6 Y-6.5
X-7 Y-6.5
X-7 Y6.5
X-8 Y6.5
X-8 Y-6.5
```

X-9 Y-6.5
X-9 Y6.5
X-10 Y6.5
X-10 Y-6.5
X-11 Y-6.5
X-11 Y6.5
X-12 Y6.5
X-12 Y-6.5
X-13 Y-6.5
X-13 Y6.5
X-14 Y6.5
X-14 Y-6.5
X-15 Y-6.5
X-15 Y6.5
X-16 Y6.5
X-16 Y-6.5
X-17 Y-6.5
X-17 Y6.5
X-18 Y6.5
X-18 Y-6.5
X-19 Y-6.5
X-19 Y6.5
X-20 Y6.5
X-20 Y-6.5
X-21 Y-6.5
X-21 Y6.5
X-22 Y6.5
X-22 Y-6.5
M96
G0 Z0.3
(Ending [Object 01-Group 01-Level 02-Layer 03])

(Beginning [Object 01-Group 01-Level 01-Layer 02])
G0 Z0.5
G0 X-23 Y5.5
G0 Z0.4
M97
G1 X23 Y5.5
X23 Y4.5
X-23 Y4.5
X-23 Y3.5
X23 Y3.5
X23 Y2.5
X-23 Y2.5
X-23 Y1.5
X23 Y1.5
X23 Y0.5
X-23 Y0.5
X-23 Y-0.5
X23 Y-0.5
X23 Y-1.5
X-23 Y-1.5
X-23 Y-2.5
X23 Y-2.5
X23 Y-3.5
X-23 Y-3.5
X-23 Y-4.5
X23 Y-4.5
X23 Y-5.5
X-23 Y-5.5

X-23 Y-6.5
X23 Y-6.5
M96
G0 Z0.5
(Ending [Object 01-Group 01-Level 01-Layer 02])

(Beginning [Object 01-Group 01-Level 02-Layer 03])
G0 Z0.7
G0 X22 Y6.5
G0 Z0.6
M97
G1 X22 Y-6.5
X21 Y-6.5
X21 Y6.5
X20 Y6.5
X20 Y-6.5
X19 Y-6.5
X19 Y6.5
X18 Y6.5
X18 Y-6.5
X17 Y-6.5
X17 Y6.5
X16 Y6.5
X16 Y-6.5
X15 Y-6.5
X15 Y6.5
X14 Y6.5
X14 Y-6.5
X13 Y-6.5
X13 Y6.5
X12 Y6.5
X12 Y-6.5
X11 Y-6.5
X11 Y6.5
X10 Y6.5
X10 Y-6.5
X9 Y-6.5
X9 Y6.5
X8 Y6.5
X8 Y-6.5
X7 Y-6.5
X7 Y6.5
X6 Y6.5
X6 Y-6.5
X5 Y-6.5
X5 Y6.5
X4 Y6.5
X4 Y-6.5
X3 Y-6.5
X3 Y6.5
X2 Y6.5
X2 Y-6.5
X1 Y-6.5
X1 Y6.5
X0 Y6.5
X0 Y-6.5
X-1 Y-6.5
X-1 Y6.5
X-2 Y6.5
X-2 Y-6.5

X-3 Y-6.5
X-3 Y6.5
X-4 Y6.5
X-4 Y-6.5
X-5 Y-6.5
X-5 Y6.5
X-6 Y6.5
X-6 Y-6.5
X-7 Y-6.5
X-7 Y6.5
X-8 Y6.5
X-8 Y-6.5
X-9 Y-6.5
X-9 Y6.5
X-10 Y6.5
X-10 Y-6.5
X-11 Y-6.5
X-11 Y6.5
X-12 Y6.5
X-12 Y-6.5
X-13 Y-6.5
X-13 Y6.5
X-14 Y6.5
X-14 Y-6.5
X-15 Y-6.5
X-15 Y6.5
X-16 Y6.5
X-16 Y-6.5
X-17 Y-6.5
X-17 Y6.5
X-18 Y6.5
X-18 Y-6.5
X-19 Y-6.5
X-19 Y6.5
X-20 Y6.5
X-20 Y-6.5
X-21 Y-6.5
X-21 Y6.5
X-22 Y6.5
X-22 Y-6.5
M96
G0 Z0.7
(Ending [Object 01-Group 01-Level 02-Layer 03])

(Beginning [Object 01-Group 01-Level 01-Layer 02])
G0 Z0.9
G0 X-23 Y5.5
G0 Z0.8
M97
G1 X23 Y5.5
X23 Y4.5
X-23 Y4.5
X-23 Y3.5
X23 Y3.5
X23 Y2.5
X-23 Y2.5
X-23 Y1.5
X23 Y1.5
X23 Y0.5
X-23 Y0.5

X-23 Y-0.5
X23 Y-0.5
X23 Y-1.5
X-23 Y-1.5
X-23 Y-2.5
X23 Y-2.5
X23 Y-3.5
X-23 Y-3.5
X-23 Y-4.5
X23 Y-4.5
X23 Y-5.5
X-23 Y-5.5
X-23 Y-6.5
X23 Y-6.5
M96
G0 Z0.9
(Ending [Object 01-Group 01-Level 01-Layer 02])

(Beginning [Object 01-Group 01-Level 02-Layer 03])
G0 Z1.1
G0 X22 Y6.5
G0 Z1
M97
G1 X22 Y-6.5
X21 Y-6.5
X21 Y6.5
X20 Y6.5
X20 Y-6.5
X19 Y-6.5
X19 Y6.5
X18 Y6.5
X18 Y-6.5
X17 Y-6.5
X17 Y6.5
X16 Y6.5
X16 Y-6.5
X15 Y-6.5
X15 Y6.5
X14 Y6.5
X14 Y-6.5
X13 Y-6.5
X13 Y6.5
X12 Y6.5
X12 Y-6.5
X11 Y-6.5
X11 Y6.5
X10 Y6.5
X10 Y-6.5
X9 Y-6.5
X9 Y6.5
X8 Y6.5
X8 Y-6.5
X7 Y-6.5
X7 Y6.5
X6 Y6.5
X6 Y-6.5
X5 Y-6.5
X5 Y6.5
X4 Y6.5
X4 Y-6.5

```
X3 Y-6.5
X3 Y6.5
X2 Y6.5
X2 Y-6.5
X1 Y-6.5
X1 Y6.5
X0 Y6.5
X0 Y-6.5
X-1 Y-6.5
X-1 Y6.5
X-2 Y6.5
X-2 Y-6.5
X-3 Y-6.5
X-3 Y6.5
X-4 Y6.5
X-4 Y-6.5
X-5 Y-6.5
X-5 Y6.5
X-6 Y6.5
X-6 Y-6.5
X-7 Y-6.5
X-7 Y6.5
X-8 Y6.5
X-8 Y-6.5
X-9 Y-6.5
X-9 Y6.5
X-10 Y6.5
X-10 Y-6.5
X-11 Y-6.5
X-11 Y6.5
X-12 Y6.5
X-12 Y-6.5
X-13 Y-6.5
X-13 Y6.5
X-14 Y6.5
X-14 Y-6.5
X-15 Y-6.5
X-15 Y6.5
X-16 Y6.5
X-16 Y-6.5
X-17 Y-6.5
X-17 Y6.5
X-18 Y6.5
X-18 Y-6.5
X-19 Y-6.5
X-19 Y6.5
X-20 Y6.5
X-20 Y-6.5
X-21 Y-6.5
X-21 Y6.5
X-22 Y6.5
X-22 Y-6.5
M96
G0 Z1.1
(Ending [Object 01-Group 01-Level 02-Layer 03])

(Beginning [Object 01-Group 01-Level 01-Layer 02])
G0 Z1.3
G0 X-23 Y5.5
G0 Z1.2
```

M97
G1 X23 Y5.5
X23 Y4.5
X-23 Y4.5
X-23 Y3.5
X23 Y3.5
X23 Y2.5
X-23 Y2.5
X-23 Y1.5
X23 Y1.5
X23 Y0.5
X-23 Y0.5
X-23 Y-0.5
X23 Y-0.5
X23 Y-1.5
X-23 Y-1.5
X-23 Y-2.5
X23 Y-2.5
X23 Y-3.5
X-23 Y-3.5
X-23 Y-4.5
X23 Y-4.5
X23 Y-5.5
X-23 Y-5.5
X-23 Y-6.5
X23 Y-6.5
M96
G0 Z1.3
(Ending [Object 01-Group 01-Level 01-Layer 02])

(Beginning [Object 01-Group 01-Level 02-Layer 03])
G0 Z1.5
G0 X22 Y6.5
G0 Z1.4
M97
G1 X22 Y-6.5
X21 Y-6.5
X21 Y6.5
X20 Y6.5
X20 Y-6.5
X19 Y-6.5
X19 Y6.5
X18 Y6.5
X18 Y-6.5
X17 Y-6.5
X17 Y6.5
X16 Y6.5
X16 Y-6.5
X15 Y-6.5
X15 Y6.5
X14 Y6.5
X14 Y-6.5
X13 Y-6.5
X13 Y6.5
X12 Y6.5
X12 Y-6.5
X11 Y-6.5
X11 Y6.5
X10 Y6.5
X10 Y-6.5

```
X9 Y-6.5
X9 Y6.5
X8 Y6.5
X8 Y-6.5
X7 Y-6.5
X7 Y6.5
X6 Y6.5
X6 Y-6.5
X5 Y-6.5
X5 Y6.5
X4 Y6.5
X4 Y-6.5
X3 Y-6.5
X3 Y6.5
X2 Y6.5
X2 Y-6.5
X1 Y-6.5
X1 Y6.5
X0 Y6.5
X0 Y-6.5
X-1 Y-6.5
X-1 Y6.5
X-2 Y6.5
X-2 Y-6.5
X-3 Y-6.5
X-3 Y6.5
X-4 Y6.5
X-4 Y-6.5
X-5 Y-6.5
X-5 Y6.5
X-6 Y6.5
X-6 Y-6.5
X-7 Y-6.5
X-7 Y6.5
X-8 Y6.5
X-8 Y-6.5
X-9 Y-6.5
X-9 Y6.5
X-10 Y6.5
X-10 Y-6.5
X-11 Y-6.5
X-11 Y6.5
X-12 Y6.5
X-12 Y-6.5
X-13 Y-6.5
X-13 Y6.5
X-14 Y6.5
X-14 Y-6.5
X-15 Y-6.5
X-15 Y6.5
X-16 Y6.5
X-16 Y-6.5
X-17 Y-6.5
X-17 Y6.5
X-18 Y6.5
X-18 Y-6.5
X-19 Y-6.5
X-19 Y6.5
X-20 Y6.5
X-20 Y-6.5
```

X-21 Y-6.5
X-21 Y6.5
X-22 Y6.5
X-22 Y-6.5
M96
G0 Z1.5
(Ending [Object 01-Group 01-Level 02-Layer 03])

(Beginning [Object 01-Group 01-Level 01-Layer 02])
G0 Z1.7
G0 X-23 Y5.5
G0 Z1.6
M97
G1 X23 Y5.5
X23 Y4.5
X-23 Y4.5
X-23 Y3.5
X23 Y3.5
X23 Y2.5
X-23 Y2.5
X-23 Y1.5
X23 Y1.5
X23 Y0.5
X-23 Y0.5
X-23 Y-0.5
X23 Y-0.5
X23 Y-1.5
X-23 Y-1.5
X-23 Y-2.5
X23 Y-2.5
X23 Y-3.5
X-23 Y-3.5
X-23 Y-4.5
X23 Y-4.5
X23 Y-5.5
X-23 Y-5.5
X-23 Y-6.5
X23 Y-6.5
M96
G0 Z1.7
(Ending [Object 01-Group 01-Level 01-Layer 02])

(Beginning [Object 01-Group 01-Level 02-Layer 03])
G0 Z1.9
G0 X22 Y6.5
G0 Z1.8
M97
G1 X22 Y-6.5
X21 Y-6.5
X21 Y6.5
X20 Y6.5
X20 Y-6.5
X19 Y-6.5
X19 Y6.5
X18 Y6.5
X18 Y-6.5
X17 Y-6.5
X17 Y6.5
X16 Y6.5
X16 Y-6.5

X15 Y-6.5
X15 Y6.5
X14 Y6.5
X14 Y-6.5
X13 Y-6.5
X13 Y6.5
X12 Y6.5
X12 Y-6.5
X11 Y-6.5
X11 Y6.5
X10 Y6.5
X10 Y-6.5
X9 Y-6.5
X9 Y6.5
X8 Y6.5
X8 Y-6.5
X7 Y-6.5
X7 Y6.5
X6 Y6.5
X6 Y-6.5
X5 Y-6.5
X5 Y6.5
X4 Y6.5
X4 Y-6.5
X3 Y-6.5
X3 Y6.5
X2 Y6.5
X2 Y-6.5
X1 Y-6.5
X1 Y6.5
X0 Y6.5
X0 Y-6.5
X-1 Y-6.5
X-1 Y6.5
X-2 Y6.5
X-2 Y-6.5
X-3 Y-6.5
X-3 Y6.5
X-4 Y6.5
X-4 Y-6.5
X-5 Y-6.5
X-5 Y6.5
X-6 Y6.5
X-6 Y-6.5
X-7 Y-6.5
X-7 Y6.5
X-8 Y6.5
X-8 Y-6.5
X-9 Y-6.5
X-9 Y6.5
X-10 Y6.5
X-10 Y-6.5
X-11 Y-6.5
X-11 Y6.5
X-12 Y6.5
X-12 Y-6.5
X-13 Y-6.5
X-13 Y6.5
X-14 Y6.5
X-14 Y-6.5

```
X-15 Y-6.5
X-15 Y6.5
X-16 Y6.5
X-16 Y-6.5
X-17 Y-6.5
X-17 Y6.5
X-18 Y6.5
X-18 Y-6.5
X-19 Y-6.5
X-19 Y6.5
X-20 Y6.5
X-20 Y-6.5
X-21 Y-6.5
X-21 Y6.5
X-22 Y6.5
X-22 Y-6.5
M96
G0 Z1.9
(Ending [Object 01-Group 01-Level 02-Layer 03])

(Beginning [Object 01-Group 01-Level 01-Layer 02])
G0 Z2.1
G0 X-23 Y5.5
G0 Z2
M97
G1 X23 Y5.5
X23 Y4.5
X-23 Y4.5
X-23 Y3.5
X23 Y3.5
X23 Y2.5
X-23 Y2.5
X-23 Y1.5
X23 Y1.5
X23 Y0.5
X-23 Y0.5
X-23 Y-0.5
X23 Y-0.5
X23 Y-1.5
X-23 Y-1.5
X-23 Y-2.5
X23 Y-2.5
X23 Y-3.5
X-23 Y-3.5
X-23 Y-4.5
X23 Y-4.5
X23 Y-5.5
X-23 Y-5.5
X-23 Y-6.5
X23 Y-6.5
M96
G0 Z2.1
(Ending [Object 01-Group 01-Level 01-Layer 02])

(Beginning [Object 01-Group 01-Level 02-Layer 03])
G0 Z2.3
G0 X22 Y6.5
G0 Z2.2
M97
G1 X22 Y-6.5
```

X21 Y-6.5
X21 Y6.5
X20 Y6.5
X20 Y-6.5
X19 Y-6.5
X19 Y6.5
X18 Y6.5
X18 Y-6.5
X17 Y-6.5
X17 Y6.5
X16 Y6.5
X16 Y-6.5
X15 Y-6.5
X15 Y6.5
X14 Y6.5
X14 Y-6.5
X13 Y-6.5
X13 Y6.5
X12 Y6.5
X12 Y-6.5
X11 Y-6.5
X11 Y6.5
X10 Y6.5
X10 Y-6.5
X9 Y-6.5
X9 Y6.5
X8 Y6.5
X8 Y-6.5
X7 Y-6.5
X7 Y6.5
X6 Y6.5
X6 Y-6.5
X5 Y-6.5
X5 Y6.5
X4 Y6.5
X4 Y-6.5
X3 Y-6.5
X3 Y6.5
X2 Y6.5
X2 Y-6.5
X1 Y-6.5
X1 Y6.5
X0 Y6.5
X0 Y-6.5
X-1 Y-6.5
X-1 Y6.5
X-2 Y6.5
X-2 Y-6.5
X-3 Y-6.5
X-3 Y6.5
X-4 Y6.5
X-4 Y-6.5
X-5 Y-6.5
X-5 Y6.5
X-6 Y6.5
X-6 Y-6.5
X-7 Y-6.5
X-7 Y6.5
X-8 Y6.5
X-8 Y-6.5

X-9 Y-6.5
X-9 Y6.5
X-10 Y6.5
X-10 Y-6.5
X-11 Y-6.5
X-11 Y6.5
X-12 Y6.5
X-12 Y-6.5
X-13 Y-6.5
X-13 Y6.5
X-14 Y6.5
X-14 Y-6.5
X-15 Y-6.5
X-15 Y6.5
X-16 Y6.5
X-16 Y-6.5
X-17 Y-6.5
X-17 Y6.5
X-18 Y6.5
X-18 Y-6.5
X-19 Y-6.5
X-19 Y6.5
X-20 Y6.5
X-20 Y-6.5
X-21 Y-6.5
X-21 Y6.5
X-22 Y6.5
X-22 Y-6.5
M96
G0 Z2.3
(Ending [Object 01-Group 01-Level 02-Layer 03])

(Beginning [Object 01-Group 01-Level 01-Layer 02])
G0 Z2.5
G0 X-23 Y5.5
G0 Z2.4
M97
G1 X23 Y5.5
X23 Y4.5
X-23 Y4.5
X-23 Y3.5
X23 Y3.5
X23 Y2.5
X-23 Y2.5
X-23 Y1.5
X23 Y1.5
X23 Y0.5
X-23 Y0.5
X-23 Y-0.5
X23 Y-0.5
X23 Y-1.5
X-23 Y-1.5
X-23 Y-2.5
X23 Y-2.5
X23 Y-3.5
X-23 Y-3.5
X-23 Y-4.5
X23 Y-4.5
X23 Y-5.5
X-23 Y-5.5

X-23 Y-6.5
X23 Y-6.5
M96
G0 Z2.5
(Ending [Object 01-Group 01-Level 01-Layer 02])

(Beginning [Object 01-Group 01-Level 02-Layer 03])
G0 Z2.7
G0 X22 Y6.5
G0 Z2.6
M97
G1 X22 Y-6.5
X21 Y-6.5
X21 Y6.5
X20 Y6.5
X20 Y-6.5
X19 Y-6.5
X19 Y6.5
X18 Y6.5
X18 Y-6.5
X17 Y-6.5
X17 Y6.5
X16 Y6.5
X16 Y-6.5
X15 Y-6.5
X15 Y6.5
X14 Y6.5
X14 Y-6.5
X13 Y-6.5
X13 Y6.5
X12 Y6.5
X12 Y-6.5
X11 Y-6.5
X11 Y6.5
X10 Y6.5
X10 Y-6.5
X9 Y-6.5
X9 Y6.5
X8 Y6.5
X8 Y-6.5
X7 Y-6.5
X7 Y6.5
X6 Y6.5
X6 Y-6.5
X5 Y-6.5
X5 Y6.5
X4 Y6.5
X4 Y-6.5
X3 Y-6.5
X3 Y6.5
X2 Y6.5
X2 Y-6.5
X1 Y-6.5
X1 Y6.5
X0 Y6.5
X0 Y-6.5
X-1 Y-6.5
X-1 Y6.5
X-2 Y6.5
X-2 Y-6.5

X-3 Y-6.5
X-3 Y6.5
X-4 Y6.5
X-4 Y-6.5
X-5 Y-6.5
X-5 Y6.5
X-6 Y6.5
X-6 Y-6.5
X-7 Y-6.5
X-7 Y6.5
X-8 Y6.5
X-8 Y-6.5
X-9 Y-6.5
X-9 Y6.5
X-10 Y6.5
X-10 Y-6.5
X-11 Y-6.5
X-11 Y6.5
X-12 Y6.5
X-12 Y-6.5
X-13 Y-6.5
X-13 Y6.5
X-14 Y6.5
X-14 Y-6.5
X-15 Y-6.5
X-15 Y6.5
X-16 Y6.5
X-16 Y-6.5
X-17 Y-6.5
X-17 Y6.5
X-18 Y6.5
X-18 Y-6.5
X-19 Y-6.5
X-19 Y6.5
X-20 Y6.5
X-20 Y-6.5
X-21 Y-6.5
X-21 Y6.5
X-22 Y6.5
X-22 Y-6.5
M96
G0 Z2.7
(Ending [Object 01-Group 01-Level 02-Layer 03])

(Beginning [Object 01-Group 01-Level 01-Layer 02])
G0 Z2.9
G0 X-23 Y5.5
G0 Z2.8
M97
G1 X23 Y5.5
X23 Y4.5
X-23 Y4.5
X-23 Y3.5
X23 Y3.5
X23 Y2.5
X-23 Y2.5
X-23 Y1.5
X23 Y1.5
X23 Y0.5
X-23 Y0.5

X-23 Y-0.5
X23 Y-0.5
X23 Y-1.5
X-23 Y-1.5
X-23 Y-2.5
X23 Y-2.5
X23 Y-3.5
X-23 Y-3.5
X-23 Y-4.5
X23 Y-4.5
X23 Y-5.5
X-23 Y-5.5
X-23 Y-6.5
X23 Y-6.5
M96
G0 Z2.9
(Ending [Object 01-Group 01-Level 01-Layer 02])

(Beginning [Object 01-Group 01-Level 02-Layer 03])
G0 Z3.1
G0 X22 Y6.5
G0 Z3
M97
G1 X22 Y-6.5
X21 Y-6.5
X21 Y6.5
X20 Y6.5
X20 Y-6.5
X19 Y-6.5
X19 Y6.5
X18 Y6.5
X18 Y-6.5
X17 Y-6.5
X17 Y6.5
X16 Y6.5
X16 Y-6.5
X15 Y-6.5
X15 Y6.5
X14 Y6.5
X14 Y-6.5
X13 Y-6.5
X13 Y6.5
X12 Y6.5
X12 Y-6.5
X11 Y-6.5
X11 Y6.5
X10 Y6.5
X10 Y-6.5
X9 Y-6.5
X9 Y6.5
X8 Y6.5
X8 Y-6.5
X7 Y-6.5
X7 Y6.5
X6 Y6.5
X6 Y-6.5
X5 Y-6.5
X5 Y6.5
X4 Y6.5
X4 Y-6.5

X3 Y-6.5
X3 Y6.5
X2 Y6.5
X2 Y-6.5
X1 Y-6.5
X1 Y6.5
X0 Y6.5
X0 Y-6.5
X-1 Y-6.5
X-1 Y6.5
X-2 Y6.5
X-2 Y-6.5
X-3 Y-6.5
X-3 Y6.5
X-4 Y6.5
X-4 Y-6.5
X-5 Y-6.5
X-5 Y6.5
X-6 Y6.5
X-6 Y-6.5
X-7 Y-6.5
X-7 Y6.5
X-8 Y6.5
X-8 Y-6.5
X-9 Y-6.5
X-9 Y6.5
X-10 Y6.5
X-10 Y-6.5
X-11 Y-6.5
X-11 Y6.5
X-12 Y6.5
X-12 Y-6.5
X-13 Y-6.5
X-13 Y6.5
X-14 Y6.5
X-14 Y-6.5
X-15 Y-6.5
X-15 Y6.5
X-16 Y6.5
X-16 Y-6.5
X-17 Y-6.5
X-17 Y6.5
X-18 Y6.5
X-18 Y-6.5
X-19 Y-6.5
X-19 Y6.5
X-20 Y6.5
X-20 Y-6.5
X-21 Y-6.5
X-21 Y6.5
X-22 Y6.5
X-22 Y-6.5
M96
G0 Z3.1
(Ending [Object 01-Group 01-Level 02-Layer 03])

(Beginning [Object 01-Group 01-Level 01-Layer 02])
G0 Z3.3
G0 X-23 Y5.5
G0 Z3.2

M97
G1 X23 Y5.5
X23 Y4.5
X-23 Y4.5
X-23 Y3.5
X23 Y3.5
X23 Y2.5
X-23 Y2.5
X-23 Y1.5
X23 Y1.5
X23 Y0.5
X-23 Y0.5
X-23 Y-0.5
X23 Y-0.5
X23 Y-1.5
X-23 Y-1.5
X-23 Y-2.5
X23 Y-2.5
X23 Y-3.5
X-23 Y-3.5
X-23 Y-4.5
X23 Y-4.5
X23 Y-5.5
X-23 Y-5.5
X-23 Y-6.5
X23 Y-6.5
M96
G0 Z3.3
(Ending [Object 01-Group 01-Level 01-Layer 02])

(Beginning [Object 01-Group 01-Level 02-Layer 03])
G0 Z3.5
G0 X22 Y6.5
G0 Z3.4
M97
G1 X22 Y-6.5
X21 Y-6.5
X21 Y6.5
X20 Y6.5
X20 Y-6.5
X19 Y-6.5
X19 Y6.5
X18 Y6.5
X18 Y-6.5
X17 Y-6.5
X17 Y6.5
X16 Y6.5
X16 Y-6.5
X15 Y-6.5
X15 Y6.5
X14 Y6.5
X14 Y-6.5
X13 Y-6.5
X13 Y6.5
X12 Y6.5
X12 Y-6.5
X11 Y-6.5
X11 Y6.5
X10 Y6.5
X10 Y-6.5

```
X9 Y-6.5
X9 Y6.5
X8 Y6.5
X8 Y-6.5
X7 Y-6.5
X7 Y6.5
X6 Y6.5
X6 Y-6.5
X5 Y-6.5
X5 Y6.5
X4 Y6.5
X4 Y-6.5
X3 Y-6.5
X3 Y6.5
X2 Y6.5
X2 Y-6.5
X1 Y-6.5
X1 Y6.5
X0 Y6.5
X0 Y-6.5
X-1 Y-6.5
X-1 Y6.5
X-2 Y6.5
X-2 Y-6.5
X-3 Y-6.5
X-3 Y6.5
X-4 Y6.5
X-4 Y-6.5
X-5 Y-6.5
X-5 Y6.5
X-6 Y6.5
X-6 Y-6.5
X-7 Y-6.5
X-7 Y6.5
X-8 Y6.5
X-8 Y-6.5
X-9 Y-6.5
X-9 Y6.5
X-10 Y6.5
X-10 Y-6.5
X-11 Y-6.5
X-11 Y6.5
X-12 Y6.5
X-12 Y-6.5
X-13 Y-6.5
X-13 Y6.5
X-14 Y6.5
X-14 Y-6.5
X-15 Y-6.5
X-15 Y6.5
X-16 Y6.5
X-16 Y-6.5
X-17 Y-6.5
X-17 Y6.5
X-18 Y6.5
X-18 Y-6.5
X-19 Y-6.5
X-19 Y6.5
X-20 Y6.5
X-20 Y-6.5
```

X-21 Y-6.5
X-21 Y6.5
X-22 Y6.5
X-22 Y-6.5
M96
G0 Z3.5
(Ending [Object 01-Group 01-Level 02-Layer 03])

(Beginning [Object 01-Group 01-Level 01-Layer 02])
G0 Z3.7
G0 X-23 Y5.5
G0 Z3.6
M97
G1 X23 Y5.5
X23 Y4.5
X-23 Y4.5
X-23 Y3.5
X23 Y3.5
X23 Y2.5
X-23 Y2.5
X-23 Y1.5
X23 Y1.5
X23 Y0.5
X-23 Y0.5
X-23 Y-0.5
X23 Y-0.5
X23 Y-1.5
X-23 Y-1.5
X-23 Y-2.5
X23 Y-2.5
X23 Y-3.5
X-23 Y-3.5
X-23 Y-4.5
X23 Y-4.5
X23 Y-5.5
X-23 Y-5.5
X-23 Y-6.5
X23 Y-6.5
M96
G0 Z3.7
(Ending [Object 01-Group 01-Level 01-Layer 02])

(Beginning [Object 01-Group 01-Level 02-Layer 03])
G0 Z3.9
G0 X22 Y6.5
G0 Z3.8
M97
G1 X22 Y-6.5
X21 Y-6.5
X21 Y6.5
X20 Y6.5
X20 Y-6.5
X19 Y-6.5
X19 Y6.5
X18 Y6.5
X18 Y-6.5
X17 Y-6.5
X17 Y6.5
X16 Y6.5
X16 Y-6.5

```
X15 Y-6.5
X15 Y6.5
X14 Y6.5
X14 Y-6.5
X13 Y-6.5
X13 Y6.5
X12 Y6.5
X12 Y-6.5
X11 Y-6.5
X11 Y6.5
X10 Y6.5
X10 Y-6.5
X9 Y-6.5
X9 Y6.5
X8 Y6.5
X8 Y-6.5
X7 Y-6.5
X7 Y6.5
X6 Y6.5
X6 Y-6.5
X5 Y-6.5
X5 Y6.5
X4 Y6.5
X4 Y-6.5
X3 Y-6.5
X3 Y6.5
X2 Y6.5
X2 Y-6.5
X1 Y-6.5
X1 Y6.5
X0 Y6.5
X0 Y-6.5
X-1 Y-6.5
X-1 Y6.5
X-2 Y6.5
X-2 Y-6.5
X-3 Y-6.5
X-3 Y6.5
X-4 Y6.5
X-4 Y-6.5
X-5 Y-6.5
X-5 Y6.5
X-6 Y6.5
X-6 Y-6.5
X-7 Y-6.5
X-7 Y6.5
X-8 Y6.5
X-8 Y-6.5
X-9 Y-6.5
X-9 Y6.5
X-10 Y6.5
X-10 Y-6.5
X-11 Y-6.5
X-11 Y6.5
X-12 Y6.5
X-12 Y-6.5
X-13 Y-6.5
X-13 Y6.5
X-14 Y6.5
X-14 Y-6.5
```

X-15 Y-6.5
X-15 Y6.5
X-16 Y6.5
X-16 Y-6.5
X-17 Y-6.5
X-17 Y6.5
X-18 Y6.5
X-18 Y-6.5
X-19 Y-6.5
X-19 Y6.5
X-20 Y6.5
X-20 Y-6.5
X-21 Y-6.5
X-21 Y6.5
X-22 Y6.5
X-22 Y-6.5
M96
G0 Z3.9
M98
(Ending [Object 01-Group 01-Level 02-Layer 03])

(Program-End)
G76 Z0
G0 X0 Y0
M2